frontiers in Earth Science

ORIGINAL RESEARCH
published: 20 July 2020
doi: 10.3389/feart.2020.00295

Chronology and Geomorphological Activity of the Akdag Rock Avalanche (SW Turkey)

Cihan Bayrakdar[1], Tolga Gorum[2], Zeynel Çılğın[3], Christof Vockenhuber[4], Susan Ivy-Ochs[4] and Naki Akçar[5]**

[1] Department of Geography, Istanbul University, Istanbul, Turkey, [2] Eurasia Institute of Earth Sciences, Istanbul Technical University, Istanbul, Turkey, [3] Department of Geography, Munzur University, Tunceli, Turkey, [4] Laboratory of Ion Beam Physics, ETH Zürich, Zurich, Switzerland, [5] Institute of Geological Sciences, University of Bern, Bern, Switzerland

Large rock-slope failures are among the primary geohazards in high mountain areas. These rock avalanches and rockslides constitute most of the world's largest landslide deposits. This study focuses on the formation and geomorphological activity of the Akdag landslide complex located on the southern slope of Mount Akdag, SW Turkey. We employed detailed mapping in the field, spatial and morphometric analysis using GIS and remote sensing technologies, and surface exposure dating with cosmogenic ^{36}Cl to reconstruct the chronology of the landslide complex. For the analysis of cosmogenic ^{36}Cl, we collected 18 surface samples from calcareous boulders within the landslide deposit. Our field mapping shows that the Akdag rock avalanche is a large and active slope failure developed between carbonates and flysch. The rock-avalanche deposits cover an area of 9.8 km^2 and together with the primary and secondary slope failures which form the landslide complex, cover an area of 15 km^2. The Akdag rock avalanche is one of the largest (3×10^8 m^3) known bedrock landslides in Turkey. Cosmogenic ^{36}Cl exposure ages indicate that the main collapse occurred at 8.3 ± 1.4 ka (2σ), followed by secondary failures. We dated one of the latter to 1.1 ± 0.2 ka (2σ). Based on field evidence, we surmise that increased water discharge in the springs along the carbonate-flysch contact zone played a key role in the Early Holocene failure.

Keywords: cosmogenic ^{36}Cl exposure dating, rock avalanche, Mount Akdag, Western Taurus, Holocene

OPEN ACCESS

Edited by:
Reginald Leonhard Hermanns, Geological Survey of Norway, Norway

Reviewed by:
Paula Hilger, Western Norway University of Applied Sciences, Norway
Gianluca Vignaroli, University of Bologna, Italy
Markus Schleier, Independent Researcher, Weilheim, Germany

****Correspondence:***
Cihan Bayrakdar
cihanbyr@istanbul.edu.tr
Naki Akçar
akcar@geo.unibe.ch

Specialty section:
This article was submitted to Structural Geology and Tectonics, a section of the journal Frontiers in Earth Science

Received: *03 January 2020*
Accepted: *24 June 2020*
Published: *20 July 2020*

Citation:
Bayrakdar C, Gorum T, Çılğın Z, Vockenhuber C, Ivy-Ochs S and Akçar N (2020) Chronology and Geomorphological Activity of the Akdag Rock Avalanche (SW Turkey). Front. Earth Sci. 8:295. doi: 10.3389/feart.2020.00295

INTRODUCTION

Large bedrock landslides represent an important geomorphological process in terms of the evolution of hillslopes and fluvial and glacial systems in mountainous terrains around the world (Densmore and Hovius, 2000; Korup, 2002; Korup et al., 2005; Hewitt et al., 2008; Ivy-Ochs et al., 2009; Shulmeister et al., 2009; Davies and McSaveney, 2012; Deline et al., 2015; Crosta et al., 2017; Singeisen et al., 2020). Substantial rock-slope failures are frequently observed in mountain landscapes due to the high topographic relief and hillslope gradient; such failures are sensitive to changes in the climate and tectonic stress conditions (Agliardi et al., 2009; Huggel et al., 2012). On a global scale, extensive bedrock landslides are responsible for 1–10% of Late Pleistocene and Holocene erosion (>1 mm per ka) in tectonically active mountain belts (Korup et al., 2007, among others), and their density is amplified by high topographic relief in response to fluvial and glacial

incision along inner gorges (Blöthe et al., 2015). Rock avalanches are characterized by large volume and long runouts due to their high energy and flow-like movement (e.g., Hungr and Evans, 2004).

Rock avalanche deposits are important markers to understand past climatic and geo-environmental changes in glaciated high mountainous terrain (Pánek, 2019). In addition, catastrophic rock-slope failures are strongly related to the location and orientation of faults, shear zones and bedding joints, as well as external triggering conditions (Ambrosi and Crosta, 2006; Stead and Wolter, 2015). Moreover, many studies have emphasized that large bedrock landslides observed after deglaciation are closely related to the decrease in ice load and changes associated with water table fluctuations (Gischig et al., 2011; McColl, 2012, 2015; McColl and Davies, 2013; Pánek, 2019). On the other hand, there may be delays in the reaction time of hillslope stability to paraglacial effects (McColl, 2012) leading to a significant relaxation time in mountain environments, which further underlines the importance of dynamic conditions due to the time-dependent changes of the conditional factors.

Periods of extreme precipitation and seismic triggering are also effective in rock-avalanche formation (Ivy-Ochs et al., 2017). Before the introduction of isotopic dating, it was generally accepted that most voluminous landslides in the Alps occurred immediately after deglaciation (Heim, 1932). As more Alpine rock-slope failures were dated, it became apparent that most of them occurred during Holocene; specifically, 6000 years or more after the glacier recession from the affected valleys (Prager et al., 2009; Ivy-Ochs et al., 2017). However, unlike the congeneric sections of the Alpine-Himalayan orogenic belt, there are no studies available on the nature and timing of rock avalanches at the Turkish syntax of the Alpine orogenic system. Limited studies on the occurrence and timing of bedrock landslides in the Pontide and Taurus mountains, which constitute the northern and southern margins of the Anatolian Orogenic Plateau, focus mainly on the northern margin of the plateau (i.e., Duman, 2009; Görüm, 2019).

Along the margins of the Anatolian Plateau, large bedrock landslides are more abundant on north-facing slopes of the Western and Eastern Pontides in the north of Turkey, where the slope and precipitation values are high (Görüm, 2019). Even though the southern margins of the orogenic plateau are similar to those of the Western and Eastern Pontides in terms of mean altitude, topographic gradient and precipitation values, the number of large bedrock landslides reported in the Taurus Mountains is limited (Görüm, 2019). Landslide deposits in this mountain belt are concentrated in the western sector, mainly in the Akdag Massif (**Figure 1**).

The Akdag Massif is characterized by autochthonous carbonates and shales overridden by allochthonous Jurassic and Cretaceous carbonates (**Figure 1**; Şenel, 1997). This massif was glaciated at least three times during Late Pleistocene (Bayrakdar, 2012; Sarıkaya et al., 2014). It is also karstified and bears large karstic depressions. Impermeable flysch deposit sequences underlie these karstic depressions. Karstic springs are located along the contact zone between the flysch and overlying carbonates. This contact area appears to be the major failure plane for most mass movements in the massif. The mass movements are concentrated on the eastern and southern slopes of the Akdag Massif, which creates a topographic asymmetry between the eastern and western slopes (Bayrakdar and Görüm, 2012).

The Akdag rock avalanche is one of the largest rock avalanches in the Western Taurus Mountains. Furthermore, Akdag is significant in terms of still being active. It is the source of many fatal debris flows in Saklikent Canyon, which is an important touristic site located downstream of the catchment area of the landslide complex. Our study gives new insights into the chronology and geomorphological activity of the Akdag rock avalanche and subsequent slope failures, with the aim of expanding the data catalog on Turkish rock avalanches and highlighting the complex interactions between glacial, karst and gravitational processes.

STUDY AREA

Geology

The Western Taurus constitutes an important part of the Alpine orogenic belt in the southwestern part of Anatolia. The study area was greatly affected by thrust faulting and napping movements. These movements made the structure of the rock units very complex (Şenel, 1997). The Beydag autochthonous carbonate platform, which is composed of Upper Cretaceous neritic limestone, underlies all units. The Elmalı formation (Eocene–Lower Miocene flysch), which is part of Yeşilbarak Nappe, tectonically overrides the Beydag autochthon.

The Madırkaya Formation is a member of the Lycian Nappes that consists of Middle Jurassic-Cretaceous neritic limestone (**Figures 1B,C**, **2**, and **3**; Şenel, 1997). This formation overlies the Yeşilbarak Nappe. In terms of active tectonics, the Akdag Massif is located on the western edge of the major geological structure known as the Isparta Angle in SW Anatolia, which is controlled by the Fethiye-Burdur fault zone (**Figure 1A**; Bozcu et al., 2007).

Geomorphology

Having a summit of 3014 m above sea level (a.s.l.) and bordered by faults on all sides, the Akdag Massif is stepped karst with flat surfaces at higher elevations (Doğu et al., 1999; Bayrakdar, 2012). Although it belongs to the Lycian Nappes, it lacks a thick carbonate stack (**Figure 1B**). Because thrust napping significantly shifted the stratigraphic location of the carbonates, these rocks are surrounded by insoluble clastic and ophiolitic rocks in some places (Şenel, 1997; Nazik and Tuncer, 2010; Bayrakdar, 2012).

For this reason, it is not possible to assert widespread karstification taking place with lateral and vertical continuity. In addition, active faults and continuous regional uplift prevent the establishment of a pronounced karstic base level at Akdag (Nazik and Tuncer, 2010; Bayrakdar, 2012). There are many uvalas and dolines above 2000 m a.s.l. due to the limestone lithologically having high solubility. The swallow holes and sinkholes within these karstic depressions have contributed to the formation of an improved underground drainage system since the beginning of karstification (Bayrakdar, 2012).

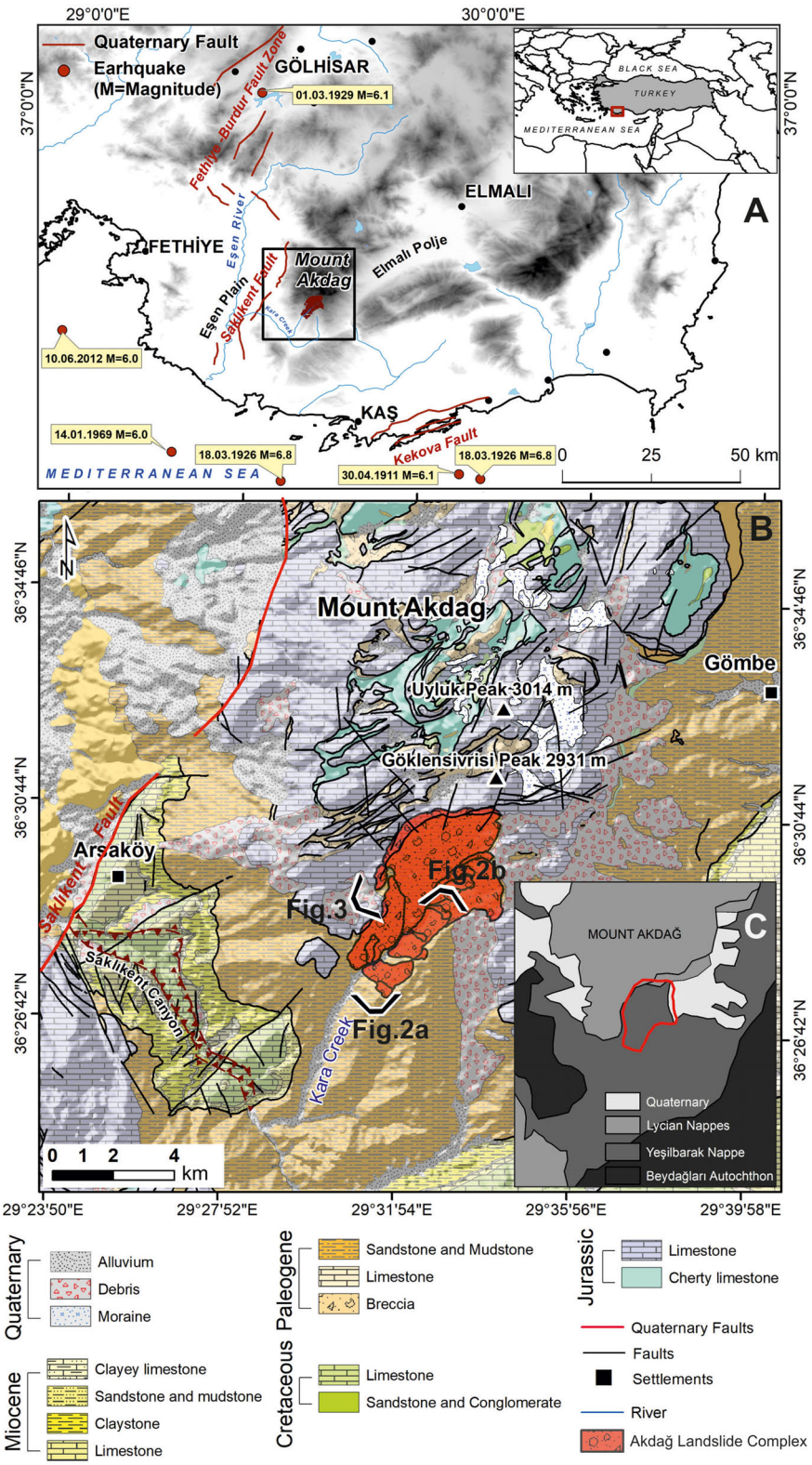

FIGURE 1 | (A) Location of Akdag Massif in southwest Turkey indicating active Quaternary faults and instrumental earthquakes and their magnitudes. **(B)** Generalized geology of Akdag Massif and its surroundings, SW Turkey (from Şenel, 1997). **(C)** Tectonic units of Mount Akdağ (from Şenel, 1997).

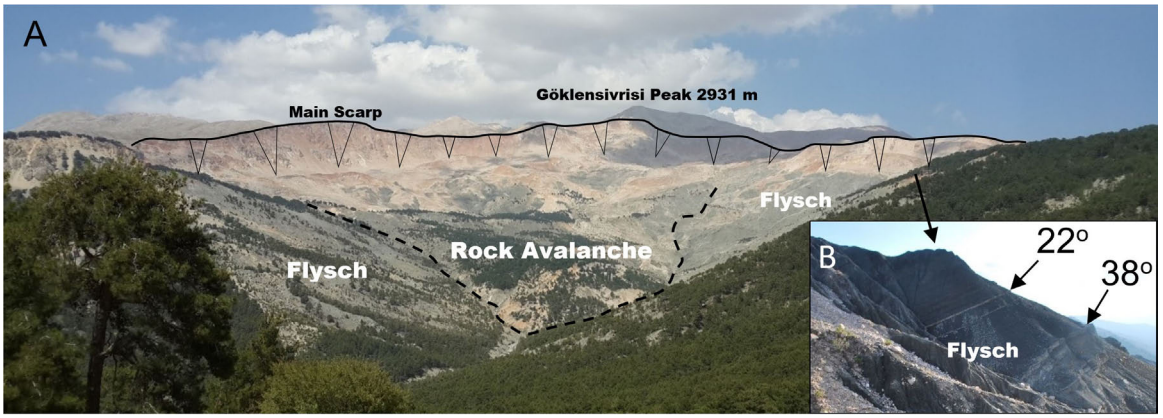

FIGURE 2 | (A) Main scarp and deposits of the rock avalanche within Akdag landslide complex, view toward north. **(B)** View of a flysch outcrop and its dip (in **Figure 1B**, viewpoint of photograph is marked).

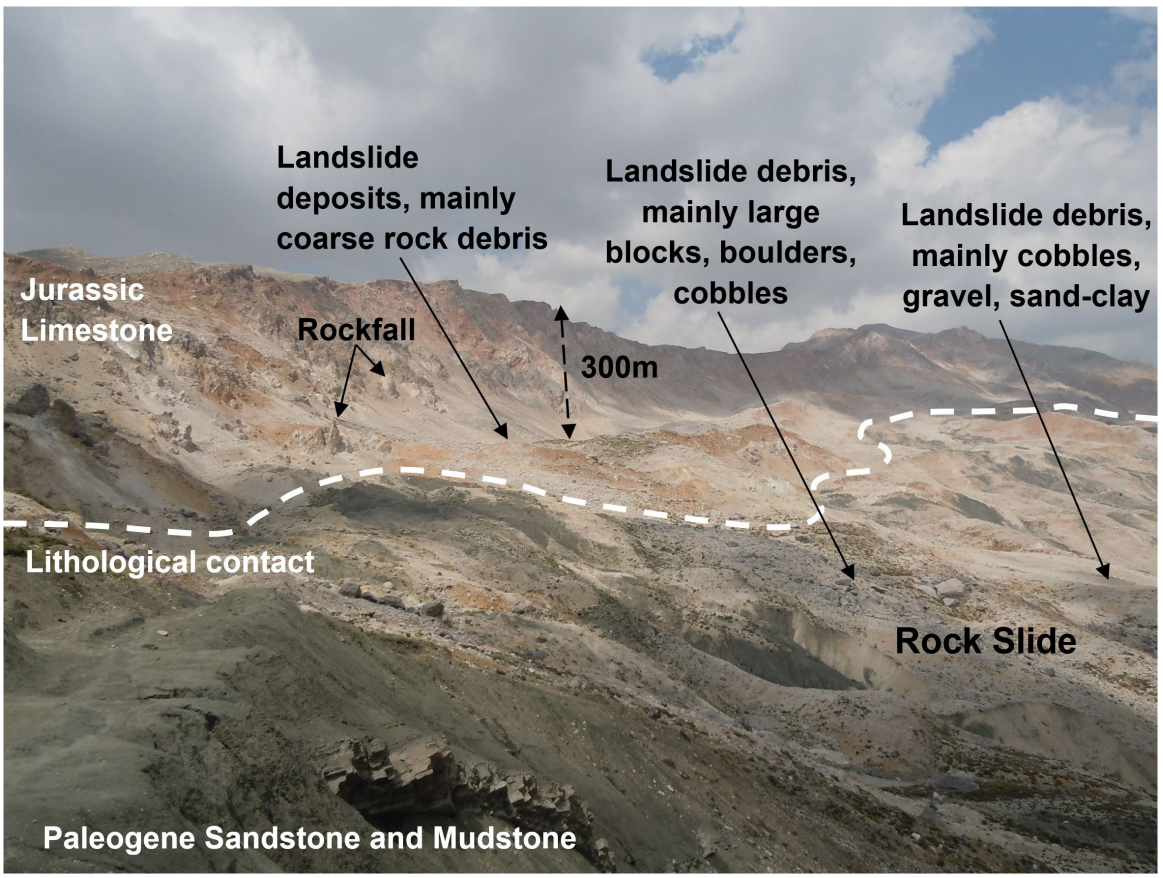

FIGURE 3 | Contact point between Jurassic limestone and Paleocene sandstone and claystone units near the head of the scarp zone of Akdag landslide complex (in **Figure 1B**, viewpoint of photograph is marked).

Mount Akdag was glaciated at least three times in Pleistocene and the associated glacial landforms were deposited by valley glaciers (Onde, 1952; Planhol and İnandık, 1958; Doğu et al., 1999; Bayrakdar, 2012; Sarıkaya et al., 2014). During the glacial advances, thick ice must have accumulated in the paleo-karstic depressions at elevations above 2500 m a.s.l. There are five glacial valleys with well-developed cirques in the Akdag Massif. These glacial valleys are in conformity with slightly inclined, wider-based paleo-karstic depressions at elevations of 2500 m, which are covered by large ground and lateral moraines. After

approximately 2500 m, these valleys start to lose their glacial morphology and become narrower and finally end at 2000 m (Bayrakdar, 2012).

The first absolute ages for the glacial chronology of the Akdag Massif were provided by Bayrakdar (2012) using the OSL dating method, for which samples were collected from terminal and ground moraines. The ages of 20.2 ± 3.0, 17.7 ± 4.4, and 17.8 ± 3.6 ka were obtained from the central part of the Akdag Massif (Bayrakdar et al., 2017). Subsequently, Sarıkaya et al. (2014) showed three glaciations and reconstructed their chronology by surface exposure dating with cosmogenic ^{36}Cl. They dated the oldest advance as prior to 35.1 ± 2.5 ka, thus before the global Last Glacial Maximum (LGM; at 22.1 + 4.3 ka in the northern hemisphere, Shakun and Carlson, 2010). They revealed that during the LGM, the glaciers reached their largest extent (descending to 2050 m a.s.l) before 21.7 ± 1.2 ka. Later, approximately 15.1 ± 0.9 ka during the Late Glacial period (Clayton et al., 2006), the glaciers retreated and remained stationary for a short period of time (Sarıkaya et al., 2017). In addition to the glacial and karst geomorphology, mass movements play a significant role in the present geomorphological appearance of Mount Akdag.

Climate

At the present time, many secondary slope instabilities are active within the Akdag landslide complex and these masses are generally accelerated by extreme rainfall and sudden snowmelt (Bayrakdar and Görüm, 2012). The Akdag Massif confronts humid air masses coming from the Mediterranean (Bayrakdar, 2012) and when moist air from the southwest reaches Akdag it is forced to ascend the hillslopes, causing orographic precipitation due to adiabatic cooling. Higher elevations of the massif receive more rainfall; whereas karstic poljes on the lee side of the Akdag Massif receive less (e.g., Elmalı Polje 470 mm; **Figure 1A**). When precipitation data from the Kaş, Fethiye and Elmalı meteorological stations near Akdag (**Figure 1A**) are extrapolated to the massif, the annual mean precipitation reaches 1200 mm at elevations above 2000 m a.s.l. From the peaks of the massif downward, the precipitation values drop to 670 mm at approximately 1000 m a.s.l. In the winter, precipitation occurs largely as snowfall in areas above 2000 m a.s.l. (Bayrakdar, 2012).

MATERIALS AND METHODS

Geomorphological and Geomorphometric Data

A geomorphological map of the Akdag landslide complex (Görüm et al., 2017) was used to characterize the Akdag rock avalanche and secondary landslides that occurred during the period following the initial failure (**Figure 4**). In addition to geomorphological mapping, the geological map of Şenel et al. (unpublished) was used to extract lithological and structural information for further interpretation. This geological map was mainly used for determining the boundaries of pre-Quaternary units. The Quaternary units were mapped by processing high-resolution remote sensing images (e.g., unmanned aerial vehicle (UAV) derived orthophoto mosaics and GeoEye-2 satellite images) as well as extensive fieldwork.

To assess the potential role of conditional factors on the occurrence of the Akdag rock avalanche and the following secondary landslide events, we obtained the following terrain metrics from a 10 m DEM of the study area in SAGA GIS(c) (Conrad et al., 2015); abundance and depth of depressions and the topographic wetness index (TWI). The closed depression map was derived using compound analyses under the terrain analysis module. The Topographic Wetness Index (TWI), which is a measure widely used to describe the effect of topography on the location and size of saturated source areas of run-off generation, was also used as a proxy for regional soil moisture assessment. We used the SAGA topographic wetness index (Olaya and Conrad, 2009), which defines TWI as:

$$\mathrm{TWI} = \mathrm{In}\left(\frac{SCA_m}{\tan(\beta)}\right) \quad (1)$$

where TWI is the SAGA wetness index at a given point, SCA_{m} is the modified specific catchment area draining to that cell, and β is the slope angle of the point (Boehner and Selige, 2006). High TWI values represent wetter conditions. After the calculation of TWI values, we then reclassified the derived results using the mean plus standard deviation (1σ) to identify particularly high values in our study area.

Surface Exposure Dating

Many landslides have been dated by cosmogenic isotopes in Europe (Ballantyne, 1998; Ivy-Ochs et al., 2009; Prager et al., 2009; Akçar et al., 2012a; Singeisen et al., 2020, among others), North America (e.g., Nichols et al., 2006), South America (e.g., Hermanns et al., 2004) and Asia (e.g., Barnard et al., 2001). The top surfaces of boulders in a landslide deposit represent potential sample locations for cosmogenic nuclide dating (Ivy-Ochs and Schaller, 2010; Pánek, 2015). Apparent exposure ages from such surfaces may be older or younger than the true deposition age (e.g., Akçar et al., 2011).

The presence of inherited nuclides from pre-failure exposure may give exposure ages that are too old (e.g., Ivy-Ochs et al., 2009; Hilger et al., 2019). In general, inheritance occurs as a result of cosmogenic nuclide accumulation both at the surface and at depth in the bedrock before the collapse (e.g., Akçar et al., 2014). The exposure duration prior and after the collapse determines the contribution of inheritance to the overestimation of the exposure age; for instance, old landslides with short pre-failure exposure times would result in limited overestimation due to inheritance (Hilger et al., 2019). However, inheritance will make a significant contribution to the age overestimation in submillennial scale failures (Akçar et al., 2012a, 2014). As well as cosmogenic nuclide accumulation prior to failure, the reworking of previously exposed boulder surfaces can cause inheritance (Ivy-Ochs and Schaller, 2010). Underestimation of the true age is generally a result of post-depositional processes such as erosion, exhumation and toppling (e.g., Putkonen and Swanson, 2003). In addition, snow, sediment and/or vegetation cover can also cause "younger" ages than the true age (Ivy-Ochs et al., 2009).

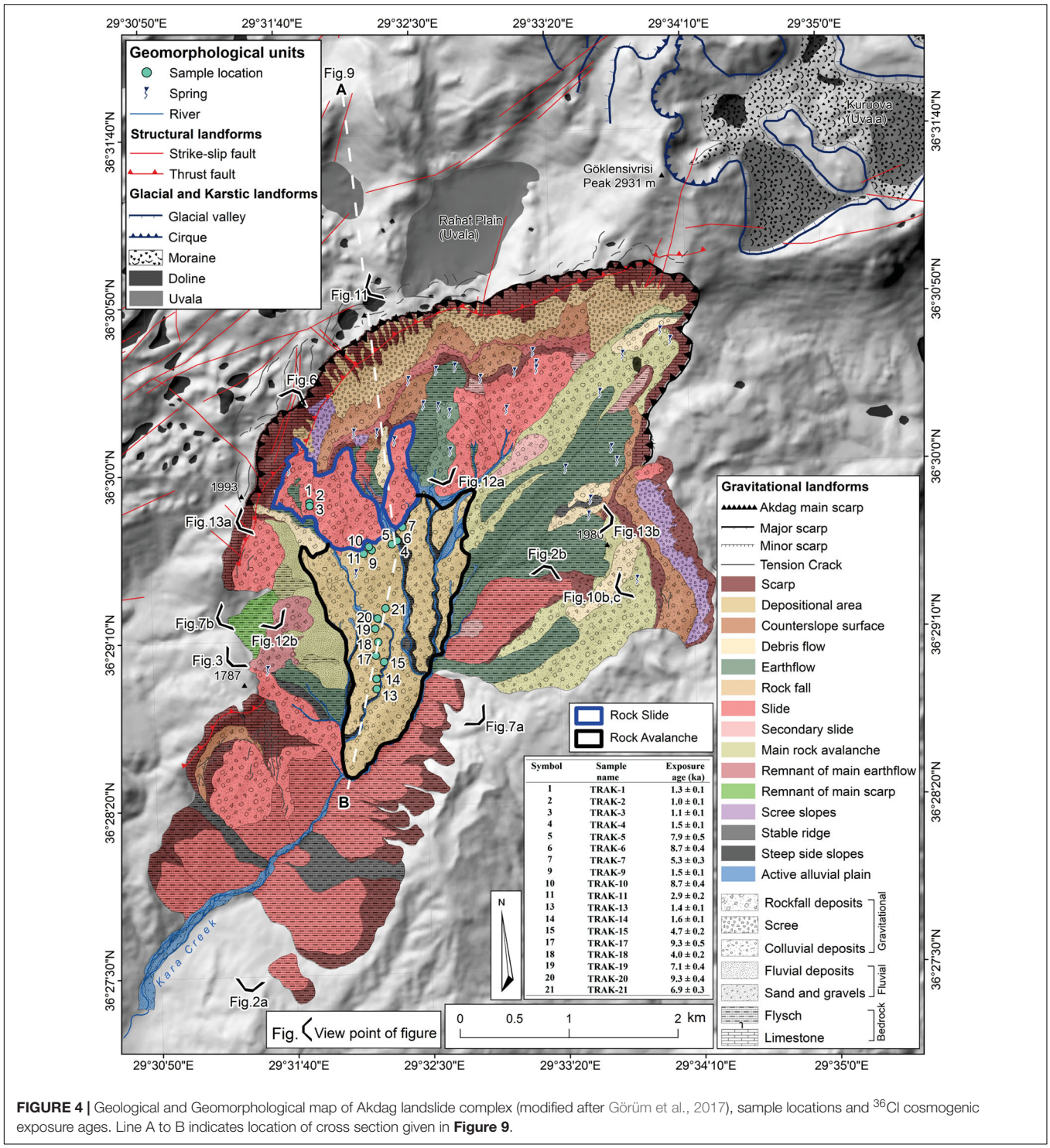

Symbol	Sample name	Exposure age (ka)
1	TRAK-1	1.3 ± 0.1
2	TRAK-2	1.0 ± 0.1
3	TRAK-3	1.1 ± 0.1
4	TRAK-4	1.5 ± 0.1
5	TRAK-5	7.9 ± 0.5
6	TRAK-6	8.7 ± 0.4
7	TRAK-7	5.3 ± 0.3
9	TRAK-9	1.5 ± 0.1
10	TRAK-10	8.7 ± 0.4
11	TRAK-11	2.9 ± 0.2
13	TRAK-13	1.4 ± 0.1
14	TRAK-14	1.6 ± 0.1
15	TRAK-15	4.7 ± 0.2
17	TRAK-17	9.3 ± 0.5
18	TRAK-18	4.0 ± 0.2
19	TRAK-19	7.1 ± 0.4
20	TRAK-20	9.3 ± 0.4
21	TRAK-21	6.9 ± 0.3

FIGURE 4 | Geological and Geomorphological map of Akdag landslide complex (modified after Görüm et al., 2017), sample locations and ^{36}Cl cosmogenic exposure ages. Line A to B indicates location of cross section given in **Figure 9**.

In this study, 18 surface samples were taken from boulders on the Akdag landslide complex (**Figures 4**, **5**). These samples were prepared at the Surface Exposure Dating Laboratory at the University of Bern following the preparation procedure described by Ivy-Ochs et al. (2004, 2009), based on the method of Stone et al. (1996) using isotope dilution (Elmore et al., 1997; Ivy-Ochs et al., 2004; Desilets et al., 2006). Before crushing, each sample was cut parallel to the surface to decrease the thickness down to 1,2 cm (**Table 1**). Afterward, the samples were crushed and sieved to 250–400 μm (micrometer) grain-size fraction. They were subsequently leached two times in 2 M HNO_3 overnight and thoroughly rinsed with ultrapure water (18.2 MΩ cm) and dried overnight to free the samples of any possible meteoric Cl. An aliquot of approximately 10 g of leached material from one

FIGURE 5 | (A) Picture of boulder TRAK-10. **(B)** Close-up view of sampled top boulder surface of TRAK-10.

sample per strip was analyzed for major and trace elements at SGS Mineral Services, Toronto, Canada (**Table 2**). The leached sample was spiked with ∼2.5 mg of pure ^{35}Cl and dissolved with HNO_3 (**Table 1**). To precipitate AgCl, $AgNO_3$ was added. Sulfur in the sample, ^{36}S as an isobar of ^{36}Cl, was eliminated by precipitation of $BaSO_4$ to avoid its interference during the accelerator mass spectrometry (AMS) measurement. The ^{35}Cl- spike was used for the determination of total Cl concentration (^{35}Cl, ^{37}Cl) in the analyzed rock material (Ivy-Ochs et al., 2004, 2009). This required the calculation of (1) the ^{36}Cl concentration in the sample; (2) ^{36}Cl production rate through low-energy neutron capture by ^{35}Cl; and (3) subsurface production of non-cosmogenic ^{36}Cl. The concentrations of total Cl and ^{36}Cl were measured from one target at the ETH AMS facility by applying the isotope dilution technique (Synal et al., 1997; Ivy-Ochs et al., 2004). In this way, independent determination of total Cl on a separate sample aliquot was eliminated; this has led to crucial improvements in both the precision and sensitivity of ^{36}Cl methodology (Ivy-Ochs et al., 2004; Desilets et al., 2006). Sample ratios of ^{36}Cl/^{35}Cl were normalized to the ETH internal standard K382/4N, which has a value of ^{36}Cl/Cl = 17.36 × 10^{-12} (normalized to the Nishiizumi standard in 2009), whereas the stable ^{37}Cl/^{35}Cl ratio was normalized to the natural ratio ^{37}Cl/^{35}Cl = 31.98% of K382/4N standard and a machine blank. The sulfur correction of measured ^{36}Cl/^{35}Cl ratios was negligible (0.7% of ratios). Measured sample ^{36}Cl/^{35}Cl ratios were also corrected for a procedure blank of 8 × 10^{-15}, which amounted to a correction of less than 5% for the samples.

For the production rate of cosmogenic ^{36}Cl, we applied 48.8 ± 1.7 atoms g^{-1} of Ca a^{-1} at SLHL as the spallogenic production rate from Ca (Stone et al., 1996, 1998) and 162 ± 24 atoms g^{-1} of K a^{-1} from K (Evans et al., 1997). The Lal

TABLE 1 | Description of samples from Akdag landslide complex.

Sample name	Elevation (m a.s.l)	Latitude, °N (DD.DD) WGS84	Longitude, °E (DD.DD) WGS84	Boulder height (m)	Sample thickness (cm)	Shielding correction factor
Trak 1	1849	36.3028	29.3149	2.40	5	0.9904
Trak 2	1838	36.2951	29.3149	1.32	5	0.9904
Trak 3	1838	36.2950	29.3149	0.80	5	0.9904
Trak 4	1776	36.2933	29.3205	0.40	5	0.9627
Trak 5	1758	36.2938	29.3219	0.90	5	0.9550
Trak 6	1757	36.2939	29.3221	1.60	5	0.9550
Trak 7	1775	36.2943	29.3223	1.70	5	0.9166
Trak 9	1766	36.2938	29.3208	1.85	5	0.9336
Trak 10	1769	36.2939	29.3207	1.20	5	0.9466
Trak 11	1770	36.2937	29.3205	1.30	5	0.9500
Trak 13	1553	36.2855	29.3212	1.00	5	0.9645
Trak 14	1581	36.2858	29.3212	1.10	5	0.9717
Trak 15	1597	36.2903	29.3215	2.00	4	0.9732
Trak 17	1618	36.2905	29.3212	1.70	5	0.9665
Trak 18	1625	36.2909	29.3213	0.70	5	0.9639
Trak 19	1641	36.2913	29.3212	1.30	3	0.9662
Trak 20	1641	36.2916	29.3213	1.70	5	0.9662
Trak 21	1665	36.2919	29.3216	1.70	5	0.9467

TABLE 2 | Major and trace element data for the analyzed samples.

Sample name	Si (wt.%)	Al (wt.%)	Fe (wt.%)	Mn (ppm)	Ca (wt.%)	K (wt.%)	Ti (wt.%)	P (wt.%)	B (ppm)	Gd (ppm)	Sm (ppm)	U (ppm)	Th (ppm)
TRAK-1	0,18	0,06	<0.05	<3	39,9	<0.1	<0.01	0,041	20	0,2	<0.1	0,2	<0.1
TRAK-2	0,13	0,05	<0.05	<3	39,9	<0.1	<0.01	0,018	<10	1,9	2,5	11,8	1,6
TRAK-3	0,12	0,04	<0.05	4	39,9	<0.1	<0.01	0,019	<10	0,2	<0.1	0,1	<0.1
TRAK-4	0,23	0,09	<0.05	<3	39,4	<0.1	<0.01	<0.005	<10	0,2	0,1	0,1	<0.1
TRAK-5	0,24	0,1	<0.05	3	39,4	<0.1	<0.01	0,008	<10	0,1	<0.1	1,4	0,1
TRAK-6	0,17	0,05	<0.05	82	39,9	<0.1	<0.01	0,027	<10	0,2	0,2	<0.1	<0.1
TRAK-7	0,28	0,11	0,05	3	39,3	<0.1	<0.01	0,014	<10	0,1	<0.1	0,4	<0.1
TRAK-9	0,22	0,09	<0.05	3	40,1	<0.1	<0.01	<0.005	<10	0,1	<0.1	0,1	0,1
TRAK-10	0,26	0,1	<0.05	8	39,8	<0.1	<0.01	<0.005	<10	0,2	0,2	0,2	0,2
TRAK-11	0,16	0,08	<0.05	5	40,7	<0.1	<0.01	0,009	<10	<0.1	<0.1	1,6	<0.1
TRAK-13	0,13	0,05	<0.05	15	40,4	<0.1	<0.01	0,009	<10	0,2	0,4	0,5	0,4
TRAK-14	0,25	0,08	<0.05	7	31,7	<0.1	<0.01	<0.005	<10	<0.1	<0.1	2,6	<0.1
TRAK-15	0,11	0,05	<0.05	3	40,4	<0.1	<0.01	<0.005	<10	<0.1	<0.1	1,2	<0.1
TRAK-17	0,12	0,05	<0.05	3	40,3	<0.1	<0.01	<0.005	<10	0,2	0,3	1,3	1,1
TRAK-18	0,1	0,08	<0.05	<3	40,7	<0.1	<0.01	0,006	<10	<0.1	<0.1	0,3	<0.1
TRAK-19	0,17	0,08	<0.05	9	40,2	<0.1	<0.01	<0.005	<10	<0.1	<0.1	0,3	<0.1
TRAK-20	0,09	0,05	<0.05	<3	40,7	<0.1	<0.01	<0.005	<10	<0.1	<0.1	0,8	0,6
TRAK-21	0,15	0,07	0,76	55	39,9	<0.1	<0.01	0,009	<10	0,2	0,2	1,7	0,2

(1991)/Stone (2000) scheme was employed to scale the local ^{36}Cl production rates in order to calculate the ^{36}Cl exposure ages. A production rate of 5.3 ± 0.5 atoms (g^{-1} Ca) a^{-1} at SLHL due to muon capture was used (Stone et al., 1996, 1998). For ^{36}Cl production caused by the capture of thermal and epithermal neutrons, we applied a rate of 760 ± 150 neutrons g^{-1} a^{-1} above the surface following Liu et al. (1994) and Phillips et al. (2001) (see Alfimov and Ivy-Ochs, 2009 for further details). Major element, boron, gadolinium and samarium concentrations were used to determine the fraction of low-energy neutrons available for capture by ^{35}Cl to build ^{36}Cl (Fabryka-Martin, 1988; Phillips et al., 2001; Alfimov and Ivy-Ochs, 2009). Uranium and thorium concentrations were considered to determine the contribution of non-cosmogenic subsurface ^{36}Cl (Fabryka-Martin, 1988). In the calculation of exposure ages, topographic shielding (based on Dunne et al., 1999), sample thickness (using an exponential attenuation length of 160 g/cm^2), rock density (2.4 g/cm^3) and erosion rate (0.5 cm/ka) were considered. We selected this erosion rate according to: (1) saturated cosmogenic ^{36}Cl concentrations analyzed in massive bedrock limestone surfaces in Crete (Ivy-Ochs, Hetzel, Alfimov unpublished data) and (2) the depth of the original quarry marks on the building stones at Hattusha, the ancient Hittite capital in central Turkey (Akçar et al., 2009).

RESULTS

Morphometric Properties of the Akdag Rock Avalanche

The surface area of the Akdag landslide complex is approximately 15 km^2. The Akdag rock avalanche is a complex landslide area that developed in multiple stages and contains more than one landslide type, caused by a massive collapse in the southern sector of the mountain. The main rock avalanche covers an area of 9.8 km^2. The approximate volume of displaced material due to this large slope failure is 3×10^8 m^3, and the distance from the crown to the toe is approximately 4.5 km (**Figure 4**).

The rock avalanche occurred on the contact plane of tectonically discordant Jurassic limestone with Paleogene sandstone and claystone units (**Figures 3**, **4**). The failure was primarily affected by structural discontinuities, such as joints, cracks and faults apparent in the source area. Many of the tension cracks and fissures observed on the landslide deposits and behind the main scarp indicate that the landslide is currently in a relatively active state (**Figure 6**). The presence of newly developed failures within the landslide mass at different periods is one of the most important indicators showing that the slopes have not stabilized to date. The jagged morphology of the crown area and concave parts of the main scarp corresponding to rockfall and secondary slip indicate that the scarp becomes rejuvenated as it retrogrades, giving the landslide a retrogressive character (**Figures 4**, **6**). Moreover, the landslide complex is enlarging its extension with secondary failures (e.g., rockslides) which have been developing on the southern slopes of Akdag (Görüm et al., 2017).

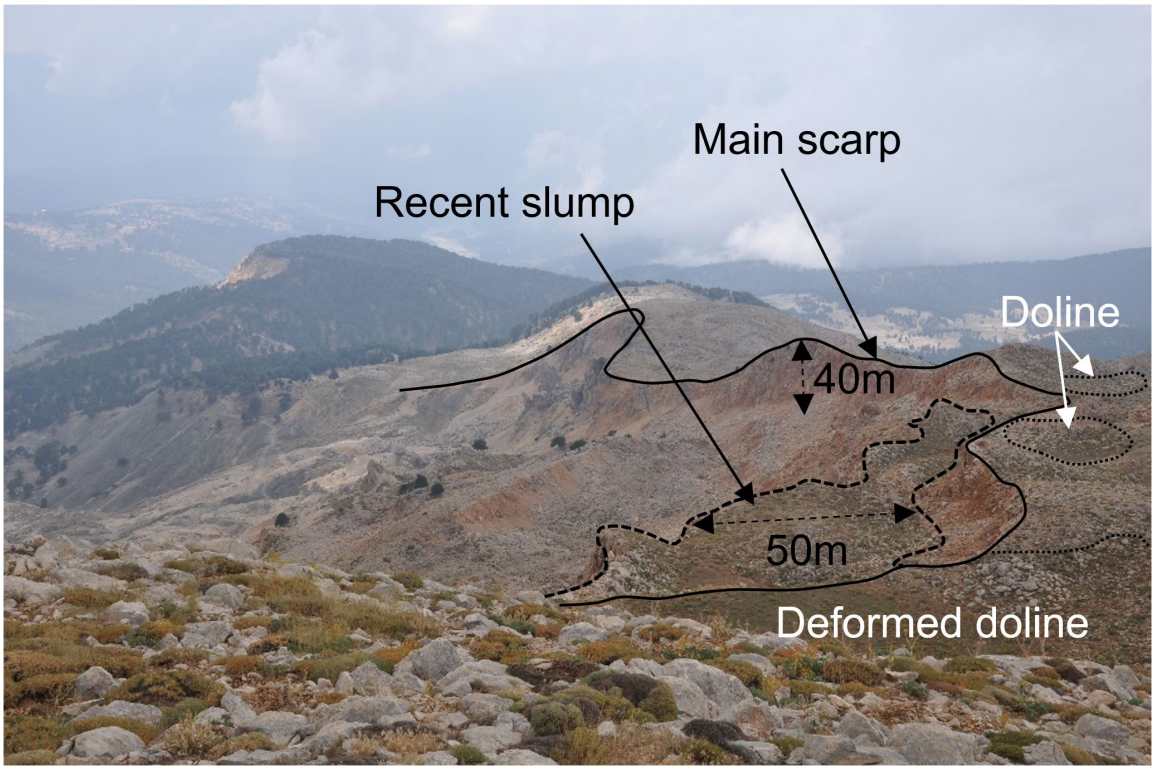

FIGURE 6 | Akdag main scarp and recent slumps inside the main scarp (in **Figure 4**, viewpoints of photographs are marked).

TABLE 3 | Cosmogenic ^{36}Cl exposure age parameters and results.

Sample name	Sample weight (g)	Carrier weight (mg)	Cl (ppm)	^{36}Cl (10^4 at.g^{-1})	Local production rate [at ^{36}Cl.g(rock).a^{-1}]	Exposure age (ka)
TRAK-1	68.9031	2.2593	63.80 ± 0.8	11.54 ± 6.9	88.54 ± 3.20	1.3 ± 0.1
TRAK-2	70.0194	2.2587	63.25 ± 1.0	8.77 ± 8.0	88.04 ± 3.19	1.0 ± 0.1
TRAK-3	70.3745	2.2542	79.49 ± 1.7	9.72 ± 8.6	91.54 ± 3.62	1.1 ± 0.1
TRAK-4	69.2951	2.2572	80.03 ± 1.3	13.03 ± 7.3	86.98 ± 3.47	1.5 ± 0.1
TRAK-5	69.1904	2.2542	93.50 ± 1.2	67.45 ± 3.8	88.28 ± 3.13	7.9 ± 0.5
TRAK-6	69.0953	2.2605	65.73 ± 1.0	69.51 ± 3.4	84.28 ± 3.17	8.7 ± 0.4
TRAK-7	68.3552	2.2623	48.69 ± 0.8	39.11 ± 3.9	81.34 ± 2.84	5.3 ± 0.3
TRAK-9	68.9534	2.2605	55.62 ± 1.1	11.50 ± 7.2	83.29 ± 2.97	1.5 ± 0.1
TRAK-10	69.1612	2.2638	54.67 ± 0.6	67.21 ± 3.0	82.90 ± 2.95	8.7 ± 0.4
TRAK-11	68.7688	2.2656	48.32 ± 1.0	22.29 ± 5.1	82.27 ± 2.85	2.9 ± 0.2
TRAK-13	69.2598	2.2626	58.80 ± 0.7	9.64 ± 7.1	72.38 ± 2.60	1.4 ± 0.1
TRAK-14	67.9544	1.9041	47.60 ± 0.8	9.03 ± 7.0	59.14 ± 2.20	1.6 ± 0.1
TRAK-15	69.3325	1.5066	38.72 ± 0.7	32.42 ± 3.9	71.58 ± 2.39	4.7 ± 0.2
TRAK-17	68.8696	2.2680	42.36 ± 0.9	64.61 ± 4.0	73.17 ± 2.48	9.3 ± 0.5
TRAK-18	68.8323	2.2536	38.72 ± 0.5	27.99 ± 4.2	72.97 ± 2.45	4.0 ± 0.2
TRAK-19	67.6867	2.2575	50.09 ± 1.3	51.54 ± 4.8	75.59 ± 2.58	7.1 ± 0.4
TRAK-20	69.2010	2.2677	31.79 ± 0.4	63.53 ± 3.1	72.68 ± 2.39	9.3 ± 0.4
TRAK-21	65.4889	2.2560	48.57 ± 0.7	48.98 ± 3.6	76.18 ± 2.62	6.9 ± 0.3

Surface Exposure Dating

Eighteen rock-surface samples were collected in Akdag from landslide deposits for cosmogenic nuclide surface exposure dating (**Table 1**). Major and trace elements measured in the collected rock surface samples are provided in **Table 2**. The cosmogenic nuclide data presented in **Table 3** are the amount of dissolved rock, the ^{35}Cl spike, total Cl concentration, ^{36}Cl concentration, local production rate of ^{36}Cl and the

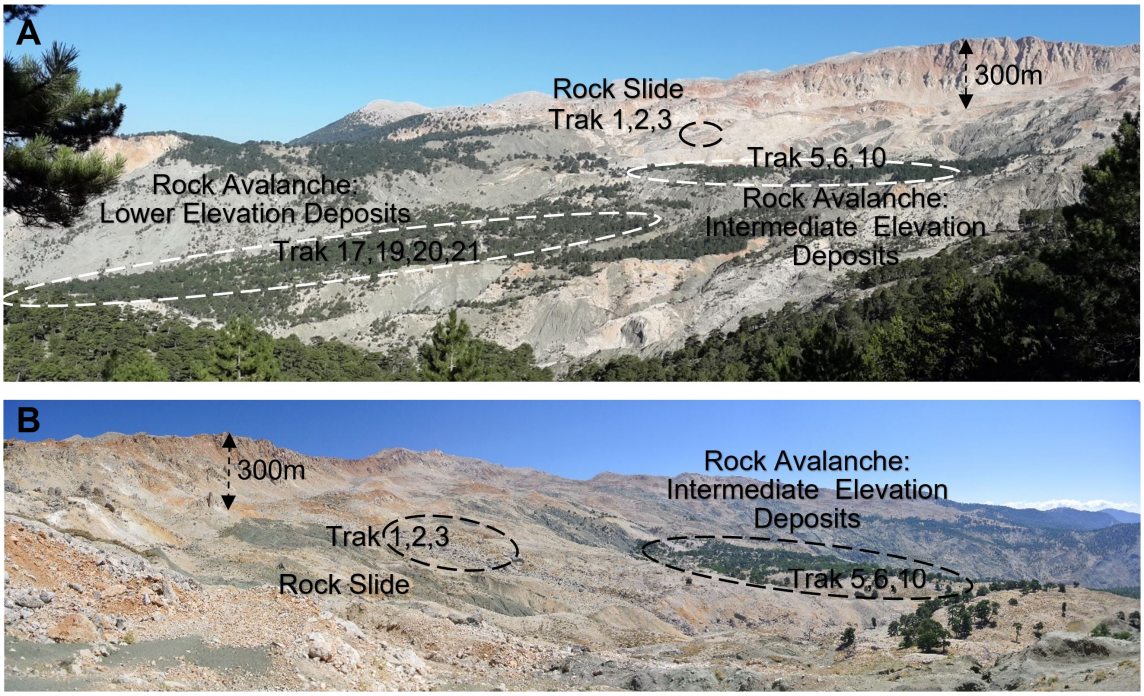

FIGURE 7 | Sampling sites for ^{36}Cl cosmogenic nuclide dating in the landslide complex. In **Figure 4**, viewpoints of photographs are marked. **(A)** Rock avalanche and rockslide. **(B)** Higher elevation deposits of rock avalanche and rockslide.

surface exposure age. The total Cl concentrations were between 31.8 ± 0.4 and 93.50 ± 1.2 ppm; and the measured ^{36}Cl concentrations were between 8.77 ± 8.0 × 10^4 atoms/g and 69.51 ± 3.4 × 10^4 atoms/g. Based on these data, we calculated ^{36}Cl exposure ages that ranged from 1.0 ± 0.1 to 9.3 ± 0.5 ka.

The deposits of the Akdag landslide complex were exposure-dated at two distinct landslide parts, consisting of a rockslide and the rock avalanche. The deposits of the latter form two topographical levels found at different levels: the intermediate elevation deposits and the lower elevation deposits (**Figure 7**). Cosmogenic ^{36}Cl exposure ages from the intermediate elevation deposits (Trak-4 to TRAK-11; **Figure 7**) of the Akdag landslide complex varied between 1.5 ± 0.1 and 8.7 ± 0.4 ka; and from the lower elevation deposits (TRAK-13 to TRAK-21; **Figure 7B**) they were between 1.4 ± 0.1 and 9.3 ± 0.5 ka, respectively. The lower elevation deposits form the lowest level of the toe of the landslide mass, which starts at 1650 m and ends at 1340 m a.s.l. then continues along a 1,900 m-long gently sloping surface. We interpret this area as being the oldest sliding section of the landslide mass, based on the exposure ages and field evidence. This part of the landslide mass has been severely dissected by streams with steep erosional slopes, indicating an absence of active movements (**Figures 4**, **8**). The oldest exposure ages are 9.3 ± 0.5 ka (TRAK-17) and 9.3 ± 0.4 ka (TRAK-20), which were collected from this level. In addition, exposure ages of 7.1 ± 0.4 (TRAK-19), 6.9 ± 0.3 (TRAK-21), 4.7 ± 0.2 (TRAK-15), 4.0 ± 0.2 ka (TRAK-18), 1.4 ± 0.1 ka (TRAK-13), and 1.6 ± 0.1 ka (TRAK-14) were also obtained from boulders on this deposit (**Figures 8**, **9**).

We explain the young exposure ages of 1.4 ± 0.1 ka (TRAK-13) and 1.6 ± 0.1 ka (TRAK-14) from the boulders situated at the lowest level of the main landslide close to the toe as follows: these boulders might belong to a younger landslide that occurred on the right lateral slope (western hillslope) of the valley which may have slumped onto the toe of the main rock avalanche body. An alternative explanation could be their exhumation due to active disintegration of the main landslide mass since failure. For this reason, the exposure ages from boulders TRAK-13 and TRAK-14 were excluded for further discussion. In addition, we argue that the young exposure ages from the boulders TRAK-15 and TRAK-18 are the result of either exhumation or surface weathering, which were not physically detectable in the field. Therefore, their exposure ages were also excluded.

Above this section, the intermediate elevation deposits of the rock avalanche are located at approximately 1750 m a.s.l. with an average width of 450 m. This level contains mounds with adjacent pits and a distorting trend toward the crown. The exposure ages of 8.7 ± 0.4 ka (TRAK-6), 8.7 ± 0.4 ka (TRAK-10), 7.9 ± 0.5 ka (TRAK-5), 5.3 ± 0.3 ka (TRAK-7), 2.9 ± 0.2 ka (TRAK-11) and 1.5 ± 0.1 ka (TRAK-4 and TRAK-9) were obtained from seven boulders from these intermediate elevation deposits (**Figure 8**). At this level, we argue that the boulders TRAK-4, 7, 9, and 11 are outliers because of exhumation. These boulders were more likely uncovered through the erosion of the matrix or exposed by secondary post-depositional processes (cf. Akçar et al., 2011) (e.g., **Figure 6**). After identifying outliers of the rock avalanche in the lower and intermediate elevation deposits, we calculated a weighted mean age of 8.3 ± 1.4 ka (2σ uncertainty) based

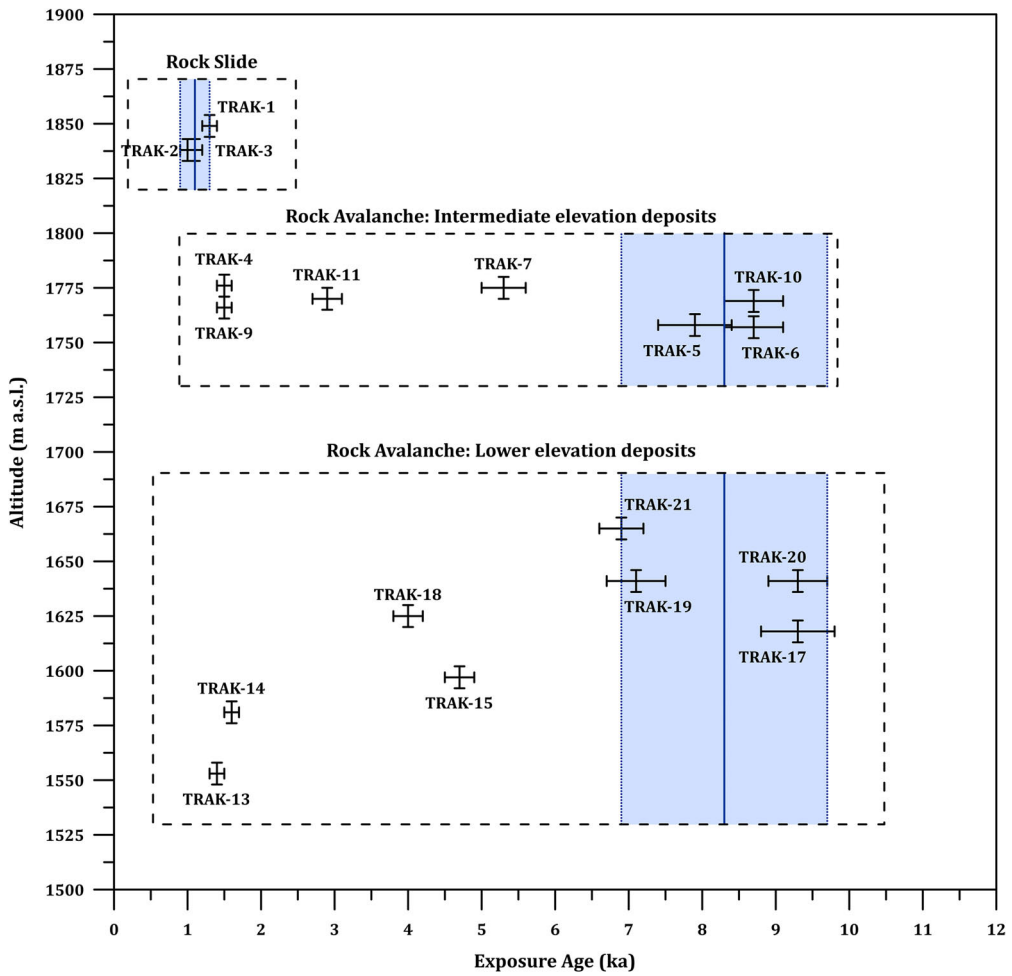

FIGURE 8 | Altitude versus cosmogenic ^{36}Cl exposure age plot. Plotted uncertainties are one sigma. Dark blue solid line indicates weighted mean ages of the rock avalanche and rockslide. Blue shaded area shows the two sigma solution space.

on the exposure ages from TRAK-5, 6, 10, 17, 19, 20, and 21, representing the entire rock avalanche body. Here, we note that the outliers plot beyond the two sigma solution space in **Figure 8**. The deposits of the secondary rockslide cover an area approximately 300 m below the crown corresponding to approximately 1850 m a.s.l., and consist of coarse debris varying from gravel to large blocks. Three surface samples collected from boulders at this site gave exposure ages of 1.1 ± 0.1 ka (TRAK-1), 1.3 ± 0.1 ka (TRAK-3), and 1.0 ± 0.1 ka (TRAK-2). Based on these exposure ages, we calculated a weighted mean age of 1.1 ± 0.2 ka (2σ uncertainty) for this rockslide (**Figure 8**).

DISCUSSION

Chronology of the Akdag Rock Avalanche and Its Plausibility

The active displacement within the Akdag landslide complex is manifested by several minor landslides along the crown of the major failure. For example, we studied one of the younger rockslides in the crown area which was dated to 1.1 ± 0.2 ka (2σ uncertainty). The toe of the rock avalanche deposits has been dissected and bears signs of disintegration as well as other geomorphic features within the complex (**Figure 4**). Our reconstructed chronology of the rock avalanche complex shows that the major collapse occurred at 8.3 ± 1.4 ka (2σ uncertainty), which we mapped as a rock avalanche. We consider that the mass of the major collapse has been actively moving since the major failure at 8.3 ± 1.4 ka. It should be noted that we cannot exclude mass wasting processes prior to 8.3 ± 1.4 ka; if the deposits were present, they were most likely overridden by a rockslide.

Surface exposure dating of landforms may sometimes be affected by inheritance (i.e., too old exposure ages) and/or exhumation (i.e., too young exposure ages) (Ivy-Ochs et al., 2007; Heyman et al., 2011, among others). However, for the following reasons, we argue that age overestimation due to inheritance in the Akdag rock avalanche is limited within the uncertainties, if present. In case of significant inheritance we would expect much older exposure ages due to the long pre-failure exposure of the study area.

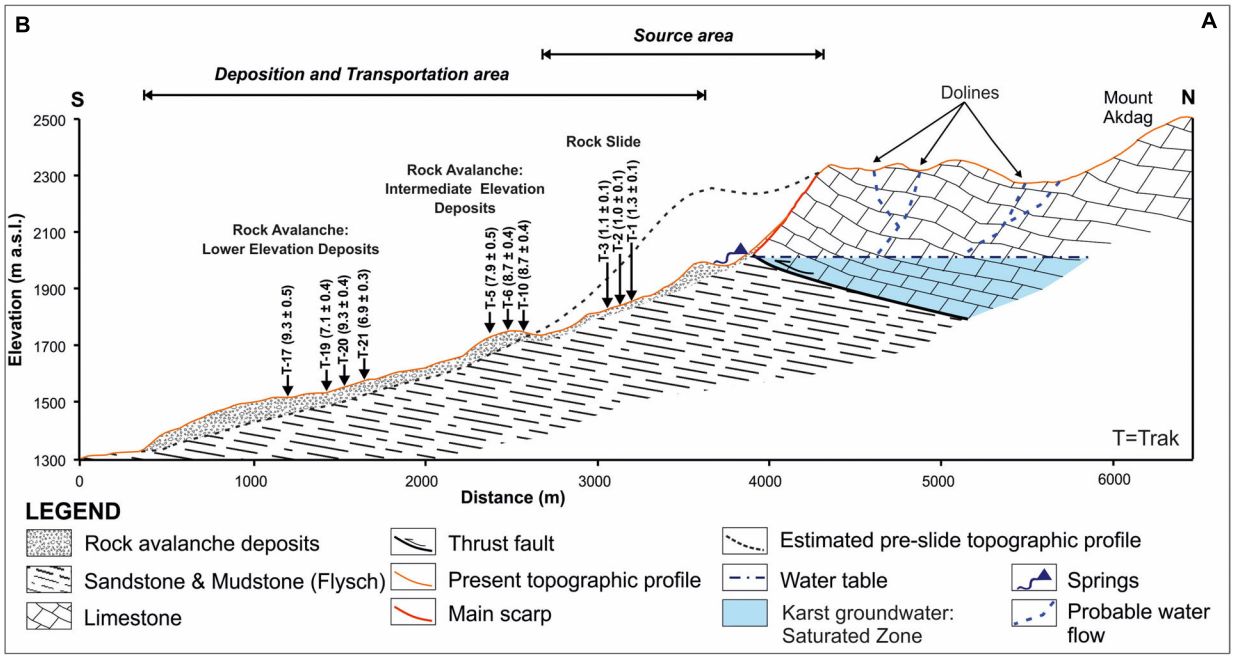

FIGURE 9 | Cross-section of Akdag rock avalanche and distribution of ^{36}Cl surface exposure ages (profile line is shown in **Figure 4** with a white dashed line).

The source area is beyond the extent of glaciations, thus the Jurassic limestone in the source area has been continuously exposed to cosmic rays during at least the last 40 ka (after Sarıkaya et al., 2014). Considering the existing chronology of the glaciations in Anatolia (Akçar et al., 2017), one could argue that the continuous exposure time is even longer, in the order of a few hundred thousand years. In both cases, the pre-collapse exposure time is long enough to cause significant inheritance. In addition, boulders which were transported on the passive carapace (Davies and McSaveney, 2009) during the collapse could certainly contain inherited cosmogenic ^{36}Cl (after Akçar et al., 2012b). Under these circumstances, we argue that we should have encountered at least one exposure age of around 20–30 ka among the 15 boulders which we sampled within the rock avalanche. It is thought that the lack of inheritance in our data might be a hint of active surface processes and/or mass wasting prior to 8.3 ± 1.4 ka.

Karstification of the Akdag Massif is still active today, which is observed in the Jurassic limestone bedrock to the north or the scarp (**Figures 3**, **6**). Similar environmental conditions are likely to have prevailed prior to the collapse, when karstification should have played a significant role in landscape degradation (Bayarı et al., 2019; Doğan et al., 2019; Nazik et al., 2019). For instance, repeated sinkhole and uvala formation and the collapse of cave systems would lead to the instantaneous removal of a few meters of rock at the surface, which would already be enough to remove the inherited cosmogenic ^{36}Cl acquired during the tens of thousands of years during the pre-collapse exposure time. In addition, repeated retrogressive wasting of the scarp area with smaller scale landslides during the pre-failure exposure time might also have contributed to the removal of inherited cosmogenic ^{36}Cl.

As well as inheritance, exhumation and/or post-depositional movement of the boulders can hinder the reconstruction of the chronology (cf. Akçar et al., 2011). In both lower and intermediate elevation deposits, eight boulders are plotted beyond the two sigma solution space. As previously explained, we argue that these boulders were exposed because of post-depositional factors, such as exhumation. In the lower elevation deposits, there is a gentle trend in the distribution of exposure ages with respect to elevation, i.e., exposure age becomes younger with decreasing elevation (**Figure 9**). This is in accordance with our field observations and interpretations. The margin (lower elevation) of the toe of the landslide mass is more unstable in comparison to the central parts (higher elevation). This indicates that post-depositional factors such as exhumation have had a potentially high effect on the boulders in this deposit. Boulders in the intermediate elevation deposits do not indicate any relationship between the elevation and exposure age (**Figure 9**) but they seem to have been affected by exhumation. They indicate a similar age distribution pattern as the lower elevation deposits; however, this resemblance does not indicate episodes of movement in the landslide mass.

The distribution of the cosmogenic ^{36}Cl exposure ages of the three boulders from the secondary rockslide shows a tight distribution (**Figure 9**). Recent slump activity has also affected the rock avalanche complex, supporting the hypothesis of a sudden secondary rock slide at 1.1 ± 0.2 ka. In these high elevation deposits, the boulders are not embedded in a matrix, which makes it unlikely that they have been shielded by sediment cover since their deposition. This field evidence points toward a lack of exhumation in this area and thus a well confined timing of failure. In general, exhumation and other post-depositional processes

in an actively moving landscape have possibly more impact on boulders than inheritance.

Causes of Akdag Rock Avalanche and Landslide Complex

The interplay of lithology, structure and surface processes is clearly complex, as multi-scale conditional factors have a destabilizing effect on rock slopes. Massive rock-slope failures such as rock avalanches are closely related with preconditioning tectonic factors; more specifically, the internal structure of hillslopes (Hermanns and Strecker, 1999; Dortch et al., 2009; Korup and Dunning, 2015). Like several reported rock avalanches in other high mountain belts around the world, the location of Akdag landslide complex is not coincidental (e.g., Davies et al., 1999; Strom and Korup, 2006).

The effects of lithological characteristics and sedimentary structures play a significant role in setting up an environment prone to slope failures in the southern section of Akdag Massif. This also affects the development of shallow karstic processes on the upper part of the Akdag rock avalanche and has formed numerous karstic depressions in the upper sections of impermeable autochthonous units (**Figure 10A**). Since nappe movements in this area significantly change the stratigraphic position of limestone units, karstic features developed horizontally due to underlying impermeable rock units. The largest of these karstic depressions is the Rahat Plain (Uvala), which has an area of 553 m^2 immediately north of the Akdag rock-avalanche scarp (**Figures 10A**, **11A**). In the formation of Rahat Plain and nearby karstic depressions, secondary inactive faults might have played a role as well as the stratigraphic position of the Elmalı formation, which acted as an impermeable zone. This impermeable unit of sandstone, claystone and siltstones builds a karstic base level; thus preventing the vertical expansion of karstification and resulting in laterally extensive and shallow karstic depressions (**Figure 10A**).

At the base of these depressions are swallow holes that drain water into the ground. Mainly during the snowmelt period, the water at the base of these karstic depressions migrates underground. The discharge most likely flows vertically until it reaches contact with the clay layers. Because of the presumed inclination of the contact zone, drainage continues toward the south along the impermeable zone of claystone and siltstones and finally emerges within the landslide complex of the massif as karstic springs. We identified numerous karstic springs emerging at the limestone-claystone contacts in the Akdag landslide complex (**Figure 10B**). Although we have no information about the density of discontinuities within the bedrock, pore-water pressures, or level of the groundwater table at the time the Akdag rock avalanche occurred, we argue that these springs are one of the crucial factors in the formation of the Akdag rock avalanche, and that they had higher flow rates at the end of the Last Glaciation and beginning of Holocene based on the spatial distribution and depth of these karstic sources (**Figure 10**).

The main rock-avalanche scarp tends to retrogressively expand to the north. Together with continuing changes in stress of the shallow karstic process after the Akdag rock avalanche, secondary slope failures were initialized, such as the analyzed rockslide, which furthered the formation of this landslide complex (**Figures 5**, **11**). Although the main scarp of the Akdag rock avalanche has not yet reached the Rahat Uvala, it has already deformed many dolines behind it (**Figures 5**, **11**). These dolines and uvalas are filled with snow in the winter period. When the snow melts during the early spring, it contributes to an increasing groundwater level that drains into the main body of the rock avalanche through subsurface drainage. In the spring, subsurface drainage enhanced by snowmelt and rainfall emerges as karstic springs at the contact plane of the Elmalı formation, just 300 m below the main scarp (**Figure 10**). Karstic springs with high flow rates and floods caused by heavy rainfall trigger rapid erosion in sandstone, claystone, and siltstone, which are easily eroded and consequently cause deep gully erosion (**Figure 12**). During floods, they rapidly erode the Elmalı formation and transform into mudflows in the creeks. This rapid erosion taking place beneath the limestone units causes further slope instability and creates new mass movements and extensive gully erosion (**Figure 13A**). Secondary slope instabilities along the main scarp form counter slopes, creating temporary ponds which in turn increase the probability of sudden failure (**Figure 13B**).

Potential Triggering Factors

Seismic shaking is one of the main factors that trigger large bedrock landslides, including rock avalanches, in tectonically active mountain belts (Keefer, 1984; Weidinger et al., 2002; Dunning et al., 2007; Görüm et al., 2014). Keefer (1984) reports that even small earthquakes (i.e., Mw 4.0) may trigger landslides; moreover, earthquakes greater than 7.0 may induce tens of thousands of landslides (Tanyas et al., 2017). The Akdag Massif is located in a tectonically active region of SW Anatolia (**Figure 1**). The neotectonic evolution of SW Anatolia is characterized by the development of several extensional intermontane basins (e.g., Esen Basin on the foothills of Akdag Massif to the west) during Late Miocene–Quaternary (e.g., Ten Veen, 2004; Alçiçek, 2007). The extensional intermountain Esen Basin includes many short normal-faulting segments running in a NE–SW direction (Emre and Duman, 2011). This fault, with a total length of 23.5 km, is known as the Saklıkent Fault, which is defined as a Quaternary fault 7.5 km west of the Akdag rock avalanche (**Figure 1A**). The fault consists of two main segments, 9.1 and 14.4 km in length, respectively.

Based on the magnitude-length scaling relationship of Wells and Coppersmith (1994), we calculated the probable earthquake magnitudes that these fault segments and the entire fault could produce if they were ruptured at once. The results showed that possible earthquake magnitudes could be M_w = 6.1, 6.4 and 6.7. Considering these magnitudes, we estimated that the maximum ground acceleration (based on the empirical equation proposed by Ulusay et al., 2004 for Turkey) that these earthquakes can produce is from 158 to 235 (gal). Paleo-earthquakes of this magnitude could potentially provide sufficient ground acceleration to trigger the Akdag rock avalanche, although there is no paleo-seismic evidence that validates this assumption. Yet further paleo-seismological investigations need to be conducted

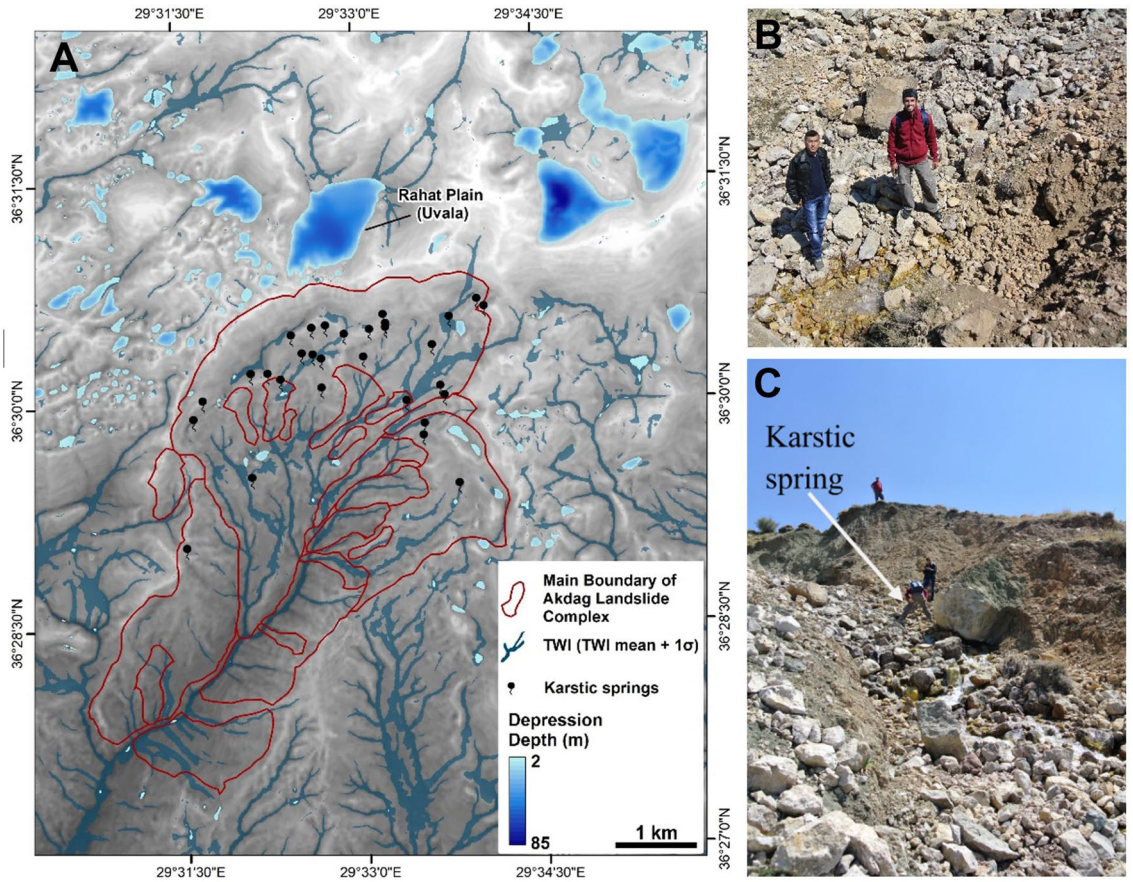

FIGURE 10 | (A) Distribution and depth of karstic depressions (TWI: topographic wetness index). **(B, C)** Head of a karstic spring on the eastern flank of the Akdag rock avalanche (In **Figure 4**, viewpoints of photographs are marked).

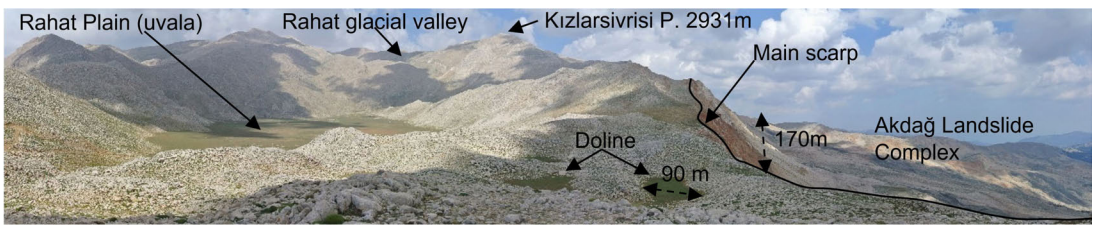

FIGURE 11 | Panoramic view of Rahat glacial valley, Rahat plain (uvala), and main scarp of the Akdag landslide south of Akdag Massif (in **Figure 4**, the viewpoints of photographs are marked).

with radiometric dating methods to clarify the role of past seismic events in the Akdag rock avalanche as a trigger factor.

Additionally, there were short cooling and warming periods during the Holocene according to research, including the study area and its near surroundings. On the basis of $\delta^{18}O$ measurements, we attempted to reveal the relationship between the landslide chronology and climate change. $\delta^{18}O$ measurements carried out in the Mediterranean (some locations close to the Akdag rock avalanche) and Black Sea basins e.g., Lake Sünnet (Ocakoğlu et al., 2013), Gölhisar (Eastwood et al., 2007), Soreq Cave (Bar-Matthews et al., 1999), Marmara Sea (Marino et al., 2009), Aegean Sea (Kotthoff et al., 2008), and Sofular Cave (Badertscher et al., 2011) indicate cooling events at 9.2, 8.9, 8.2 and 7.6 ka (Ocakoğlu et al., 2013). Among the locations mentioned above, Gölhisar is closest to Akdag, found 70 km north of the mountain. Although the $\delta^{18}O$ climate record from Gölhisar does not show a close relationship with Akdag landslide activity, isotopic fluctuations in this lake during the early-to-mid Holocene (8800–5100 ka) suggest oscillations between aridity and humidity (Eastwood et al., 2007). It can be asserted that specifically humid periods may have triggered the Akdag rock avalanche (**Figure 14**).

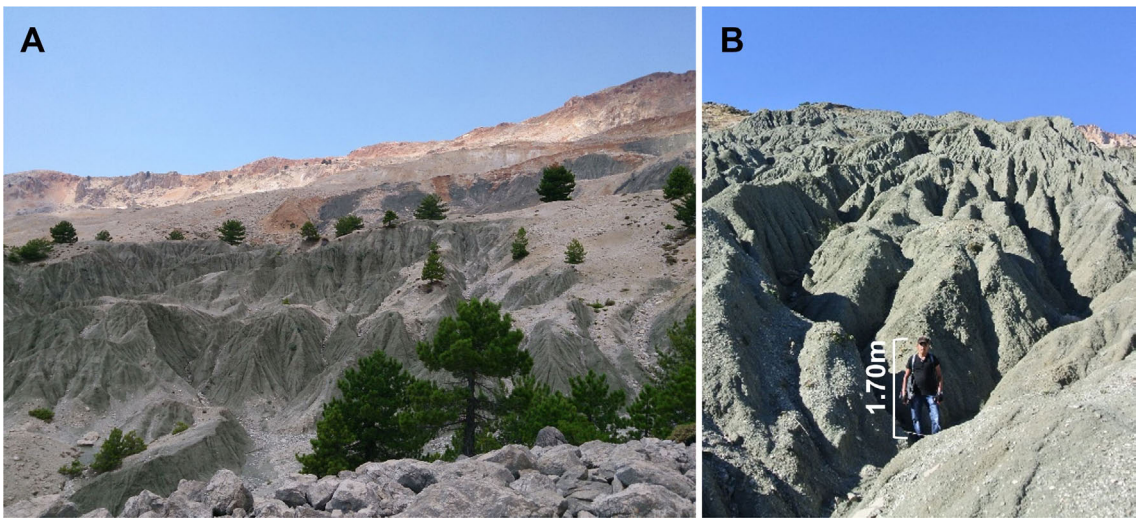

FIGURE 12 | (A) Different lithology and forms of erosion in the landslide. **(B)** Gully erosion (in **Figure 4**, the viewpoints of photographs are marked).

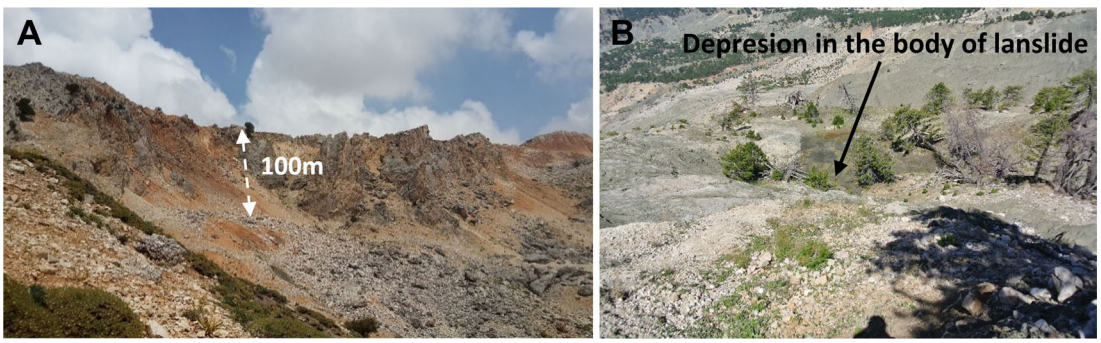

FIGURE 13 | (A) Rock slump on scarp due to slope instability. **(B)** Destruction of forest on Elmalı formation as a result of flow material in one of the secondary rock avalanches (in **Figure 4**, viewpoints of photographs are marked).

Besides the impact of past climatic events, today's climatic characteristics also cause landslide activity on Akdag. The landslide complex is found on the western part of the Teke Peninsula, surrounded by the Mediterranean. This area encounters moist air masses coming from the southwest over the Mediterranean. These air masses are confronted by the south and west slopes of Akdag Massif, as the first high and prominent mountain range on the peninsula. As the humid air ascends over the southern hillslope of the mountain where the Akdag rock avalanche is located, it is forced into lifting further and finally turns into orographic precipitation due to adiabatic cooling. The annual average precipitation reaches 1200 mm in this area (Bayrakdar, 2012), and sporadic heavy rainfall triggers many large and small landslides.

Based on the cosmogenic ^{36}Cl chronology, we concluded that the main rock avalanche occurred at 8.3 ± 1.4 ka (2σ), and a secondary rockslide at 1.1 ± 0.2 ka (2σ) (**Figures 9**, **10**). Moreover, although a clear relation between the exposure ages and the δ^{18}O climatic data cannot be established from the locations close to Akdag, a parallel relationship can be seen between the cooling periods and landslide activity. The age of 8.3 ± 1.4 ka (2σ) for the Akdag rock avalanche is more meaningful when correlated with global climate change during the Holocene (**Figure 14**). The Holocene thermal maximum was reached 9,000–5,000 years ago in the northern central Mediterranean region. The average July temperature is estimated to have been 1,2°C warmer than the recent pre-industrial period, consistent with glacier and marine records, and with transient climate model runs (Samartin et al., 2017). At the beginning of the Holocene, the increase in temperature may have triggered the Akdag rock avalanche by causing rapid melting of glaciers and snow. In particular, the glacier and snow in the glacio-karstic Kuruova uvala found to the northeast of the landslide complex may have produced enough melting water for the underground system to trigger a slope failure because the limestone strata dips toward the landslide complex (**Figure 4**).

A common pattern of landslide occurrence in previously glaciated areas is that many major landslides are of the order of 10 to 8 ka in age, with another cluster around mid-late Holocene at approximately 3–2 ka (Abele, 1997). These findings have been

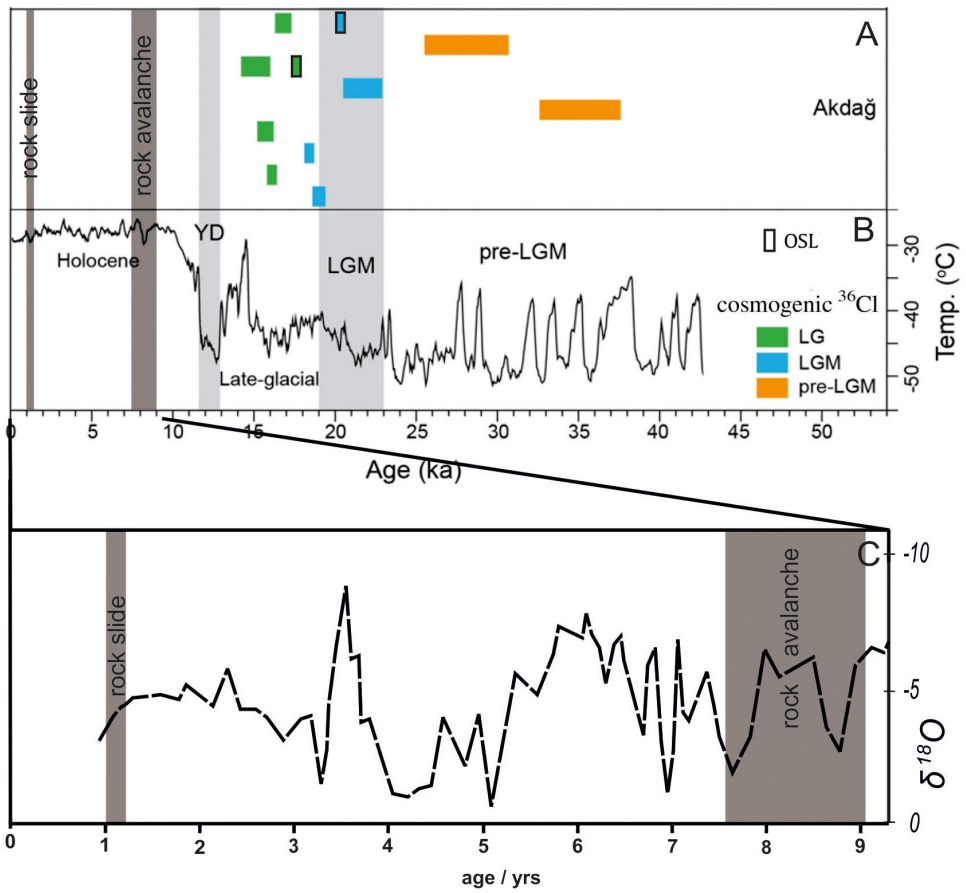

FIGURE 14 | Comparison between OSL dating (Bayrakdar, 2012; Bayrakdar et al., 2017) and cosmogenic surface exposure dating (Sarıkaya et al., 2014) for the Akdag Massif glacial chronology (Sarıkaya and Çiner, 2015). **(A)** Past surface temperatures gathered by drilling cores from Greenland GISP 2 (Alley, 2000). **(B)** Correlation between δδ18O climate data belonging to Gölhisar, located 70 km north of Akdag (Eastwood et al., 2007). **(C)** 36Cl exposure age of the rock avalanche and rockslide.

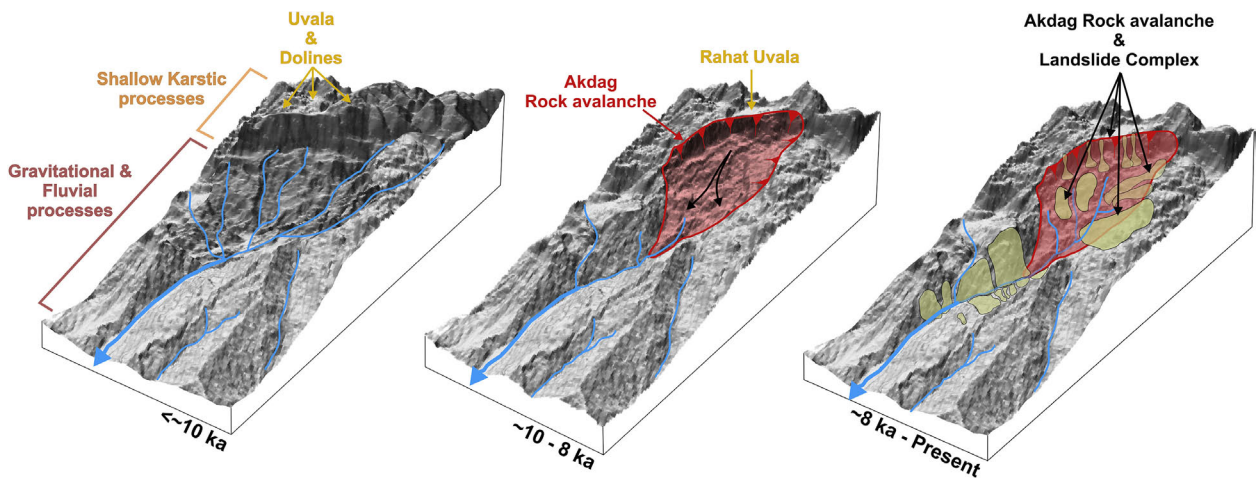

FIGURE 15 | Schematic three-dimensional diagram showing the eventual morphologic appearance before and after Akdag rock avalanche. Blue lines and arrows denote river network and flow direction, respectively.

both surprising and challenging for researchers in the European Alps, who had previously assumed that the relict large landslides were a remnant of deglaciation and not a phenomenon that had occurred under climatic conditions similar to the present (Abele, 1997). While some major landslides began occurring before deglaciation (Ambrosi and Crosta, 2006), and some were synchronous with deglaciation (Agliardi et al., 2001; Smith, 2001), the majority of documented cases indicate that large post-glacial failures typically occurred thousands of years after the retreat of the ice (McColl, 2012). Although the landslides mentioned here occurred in valleys that were glaciated during the Last Glacial (Clayton et al., 2006; Bayrakdar, 2012; Sarıkaya et al., 2014; Bayrakdar et al., 2017), the Akdag rock avalanche took place just beyond the maximum extent of the glaciers in this massif. The exposure ages have shown that the first landslide happened at c. 8.3 ka, and the second major failure came about at c. 1.1 ka. The instability after these major events led to sequential slope failures and formed the Akdag landslide complex (**Figure 15**).

CONCLUSION

Occurring on the southern slope of the Akdag Massif in the western Mediterranean region, the Akdag landslide is a complex phenomenon covering a surface area of approximately 9.8 km^2 that developed under the impetus of multiple factors and involves more than one type of movement. Because the slope failure was initiated at the point of contact between carbonates and flysch, the total mass of displaced material has been calculated as 300×10^6 m^3. This volume makes it the largest bedrock landslide known in the Western and Central Taurus mountains. The surface exposure ages show that there were two major events: the first is a rock avalanche dated to 8.3 ± 1.4 ka (2σ), and the second is a rockslide dated to 1.1 ± 0.2 ka (2σ). The rock avalanche event is closely related to karstic depressions in the upper parts of Akdag Massif and wetter conditions prevailing at the beginning of Holocene. The landslide is still active and is enlarging toward the sides and upper slopes.

Although the first major failure of the Akdag rock avalanche dates to early Holocene, the presence of new landslides observed in several field campaigns indicate that the landslide mass is currently active. As well as forested and residential areas, there are many important roads and water pipeline routes within the landslide area. Depending on the progress of landslide activity, the residential areas and roads are constantly in danger and frequently damaged causing loss of life, property and resources that cannot be recovered. Since the landslide areas may be characterized as a mountain basin providing a high input of debris into the river system, it heightens the effect of frequent torrents, especially in Saklikent Canyon, an important tourist site downstream of the basin. The fatal torrent in July 2014 triggered by a flash flood or heavy rainfall event in which two tourists died and nine people were seriously injured is only one example of the landslide geohazards posing a risk to tourists and local people (Görüm et al., 2017). In this respect, the landslide's long-term activity and the quantity of sediment flux need to be monitored. From this aspect, keeping track of current mass movements affecting the landslide, as well as the process understanding, is of great importance for local and national authorities to take preventive measures to counter landslide hazards and risks.

DATA AVAILABILITY STATEMENT

All datasets presented in this study are available upon request.

ETHICS STATEMENT

Written informed consent was obtained from the relevant individuals for the publication of any potentially identifiable images or data included in this article.

AUTHOR CONTRIBUTIONS

CB, TG, ZÇ, and NA designed the study. NA, CV, and SI-O performed the Cosmogenic Cl-36 exposure dating processing with input from CB. CB, TG, and NA wrote the manuscript with input by all co-authors. All authors interpreted and discussed the results.

ACKNOWLEDGMENTS

We would like to thank the Scientific Research Projects Coordination Unit of Istanbul University (Project number: ONAP 33594 [ID734]) for their support. We are most grateful to the Laboratory of Ion Beam Physics (accelerator mass spectrometry facility) operated by the Swiss Federal Institute of Technology, Zurich, Switzerland for the AMS measurements. We thank Dr. Nasim Mozafari for his collaboration during the sample preparation, Dr. Abdullah Akbaş and Dr. Ozan Kocadağlı for their assistance, and Mücahit Durmuş and Onur Yasan for their support during our fieldwork studies, and Graham H. Lee for proofreading. We sincerely thank the topic editors; Adrian Pfiffner, Tim Davies, John Clague, and Reginald Leonhard Hermanns and three referees for their instructive and thought-provoking comments on an earlier version of this manuscript.

REFERENCES

Abele, G. (1997). "Influence of glacier and climatic variation on rockslide activity in the Alps," in *Rapid mass movement as a source of climatic evidence for the Holocene*, Vol. 19, eds J. A. Matthews, B. Brunsden, B. Frenzel, B. Glaser, M. Weiß, and M. Palaoklimaforschung (Stuttgart: Gustav Fischer Verlag), 1–6.

Agliardi, F., Crosta, G., and Zanchi, A. (2001). Structural constraints on deep-seated slope deformation kinematics. *Eng. Geol.* 59, 83–102. doi: 10.1016/s0013-7952(00)00066-1

Agliardi, F., Crosta, G. B., Zanchi, A., and Ravazzi, C. (2009). Onset and timing of deep-seated gravitational slope deformations in the eastern Alps, Italy. *Geomorphology* 103, 113–129. doi: 10.1016/j.geomorph.2007.09.015

Akçar, N., Deline, P., Ivy-Ochs, S., Alfimov, V., Hajdas, I., Kunik, P. W., et al. (2012a). The 1717 AD rock avalanche deposits in the upper ferret valley (Italy): a datingapproach with cosmogenic 10Be. *J. Quat. Sci.* 27, 383–392. doi: 10.1002/jqs.1558

Akçar, N., Tikhomirov, D., Özkaymak, C., Ivy-Ochs, S., Alfimov, V., Sözbilir, H., et al. (2012b). 36Cl exposure of dating paleoearthquakes in the eastern mediterranean: first results from the western Anatolian Extensional Province, Manisa fault zone, Turkey. *GSA Bull.* 124, 1724–1735. doi: 10.1130/b30614.1

Akçar, N., Ivy-Ochs, S., Alfimov, V., Schlunegger, F., Claude, A., Reber, R., et al. (2017). Isochron-burial dating of glaciofluvial deposits: First results from the Swiss Alps. *Earth Surf. Process. Landf.* 42, 2414–2425. doi: 10.1002/esp.4201

Akçar, N., Ivy-Ochs, S., Alfimov, V., Yılmaz, ÝÖ, Schachner, A., Altıner, D., et al. (2009). First results on determination of cosmogenic 36Cl in limestone from the Yenicekale Complex in the Hittite capital of Hattusha (Turkey). *Quat. Geochronol.* 4, 533–540. doi: 10.1016/j.quageo.2009.09.002

Akçar, N., Ivy-Ochs, S., Kubik, P. W., and Schlüchter, C. (2011). Post-depositional ompacts on "Findlinge" (erratic boulders) and their implications for surface-exposure dating. *Swiss J. Geosci.* 104, 445–453. doi: 10.1007/s00015-011-0088-7

Akçar, N., Yavuz, V., Ivy-Ochs, S., Reber, R., Kubik, P. W., Zahno, C., et al. (2014). Glacier response to the change in atmospheric circulation in the eastern Mediterranean during the Last Glacial Maximum. *Quat. Geochronol.* 19, 27–41. doi: 10.1016/j.quageo.2013.09.004

Alçiçek, C. M. (2007). Tectonic development of an orogen-top rift recorded by its terrestrial sedimentation pattern: the Neogene Eşen Basin of southwestern Anatolia, Turkey. *Sediment. Geol.* 200, 117–140. doi: 10.1016/j.sedgeo.2007.04.003

Alfimov, V., and Ivy-Ochs, S. (2009). How well do we understand production of 36Cl in limestone and dolomite? *Quat. Geochronol.* 4, 462–474. doi: 10.1016/j.quageo.2009.08.005

Alley, R. B. (2000). The younger dryas cold interval as viewed from central greenland. *Quat. Sci. Rev.* 2013–2226.

Ambrosi, C., and Crosta, G. B. (2006). Large sackung along major tectonic features in the Central Italian Alps. *Eng. Geol.* 83, 183–200. doi: 10.1016/j.enggeo.2005.06.031

Badertscher, S., Fleitmann, D., Cheng, H., Edwards, R. L., Göktürk, O. M., Zumbühl, A., et al. (2011). Pleistocene water intrusions from the Mediterranean and Caspian seas into the Black Sea. *Nat. Geosci.* 4, 236–239. doi: 10.1038/ngeo1106

Ballantyne, C. K. (1998). Aeolian deposits on a Scottish mountain summit: characteristics, provenance, history and significance. *Earth Surf. Process. Landf.* 23, 625–641. doi: 10.1002/(sici)1096-9837(199807)23:7<625::aid-esp874>3.0.co;2-f

Bar-Matthews, M., Ayalon, A., Kaufman, A., and Wasserburg, G. (1999). The eastern Mediterranean paleoclimate as a reflection of regional events: soreq cave, Israel. *Earth Planet. Sci. Lett.* 166, 85–95. doi: 10.1016/s0012-821x(98)00275-1

Barnard, P. L., Owen, L. A., Sharma, M. C., and Finkel, R. C. (2001). Natural and humaninduced landsliding in the garhwal himalaya of northern India. *Geomorphology* 40, 21–35. doi: 10.1016/s0169-555x(01)00035-6

Bayarı, C. S., Klimchouk, A., Sarıkaya, M. A., and Nazik, L. (2019). "Aladağlar mountain range: a landscape-shaped by the interplay of glacial, karstic, and fluvial erosion," in *Landscapes and Landforms of Turkey*, eds C. Kuzucuoçlu, A. Çiner, and N. Kazancı (Cham: Springer), 423–435. doi: 10.1007/978-3-030-03515-0_22

Bayrakdar, C. (2012). *Akdağ Kütlesi'nde (Batı Toroslar) Karstlaşma-Buzul Ýlişkisinin Jeomorfolojik Analizi*. Unpublished PhD thesis., Ýstanbul University, Ýstanbul.

Bayrakdar, C., and Görüm, T. (2012). Yeşil göl heyelanı'nın jeomorfolojisi ve oluşum mekanizması. *Türk. Coğrafya Dergisi.* 1–10.

Bayrakdar, C., Güneç Kıyak, N., Turoğlu, H., Öztürk, T., and Canel, T. (2017). Akdag Kütlesi'nde (Batı Toroslar) Pleistosen buzullaşmalarının jeomorfolojik özellikleri ve optik uyarmalı lüminesans (OSL) ile yaşlandırılması. *Türk. Coğrafya Dergisi.* 27–37. doi: 10.17211/tcd.318170

Blöthe, J. H., Korup, O., and Schwanghart, W. (2015). Large landslides lie low: excess topography in the Himalaya-Karakoram ranges. *Geology* 43, 523–526. doi: 10.1130/g36527.1

Boehner, J., and Selige, T. (2006). "Spatial prediction of soil attributes using terrain analysis and climate regionalisation," in *SAGA – Analysis and Modelling Applications*, Vol. 115, eds J. Boehner, K. R. McCloy, and J. Strobl (Goettingen: Goettinger Geographische Abhandlungen), 13–28.

Bozcu, M., Yağmurlu, F., and Şentürk, M. (2007). Some neotectonic and paleosismological features of the fethiye-burdur fault zone, SWAnatolia. *Geol. Eng.* 2, 25–48.

Clayton, L., Attig, J. W., Mickelson, D. M., Johnson, M. D., and Syverson, K. M. (2006). *Glaciation of Wisconsin*. Wisconsin: Wisconsin Geological and Natural History Survey.

Conrad, O., Bechtel, B., Bock, M., Dietrich, H., Fischer, E., Gerlitz, L., et al. (2015). System for automated geoscientific analyses (SAGA) v. 2.1.4. *Geosci. Model Dev. Discuss.* 8, 2271–2312. doi: 10.5194/gmdd-8-2271-2015

Crosta, G. B., Hermanns, R. L., Dehls, J., Lari, S., and Sepulveda, S. (2017). Rock avalanches clusters along the northern Chile coastal scarp. *Geomorphology* 289, 27–43. doi: 10.1016/j.geomorph.2016.11.024

Davies, T. R., and McSaveney, M. J. (2009). The role of rock fragmentation in the motion of large landslides. *Eng. Geol.* 109, 67–79. doi: 10.1016/j.enggeo.2008.11.004

Davies, T. R., and McSaveney, M. J. (2012). *Mobility of Long-Runout Rock Avalanches. Landslides–types, Mechanisms and Modeling,* eds J. J. Clague and D. Stead. Cambridge: Cambridge University Press, 50–58.

Davies, T. R., McSaveney, M. J., and Hodgson, K. A. (1999). A fragmentation-spreading model for long-runout rock avalanches. *Can. Geotechnol. J.* 36, 1096–1110. doi: 10.1139/t99-067

Deline, P., Hewitt, K., Reznichenko, N., and Shugar, D. (2015). Rock avalanches onto glaciers. *Landslide Hazards Risks Disasters* 2015, 263–319. doi: 10.1016/b978-0-12-396452-6.00009-4

Densmore, A. F., and Hovius, N. (2000). Topographic fingerprint of bedrock landslides. *Geology* 28, 371–374. doi: 10.1130/0091-7613(2000)028<0371:tfobl>2.3.co;2

Desilets, D., Zreda, M., Almasi, P. F., and Elmore, D. (2006). Desilets, D., Zreda, MDetermination of cosmogenic Cl-36 in rocks by isotope dilution: innovations, validation and error propagation. *Chem. Geol.* 123, 185–195. doi: 10.1016/j.chemgeo.2006.03.001

Doğan, U., Koçyiğit, A., and Yeşilyurt, S. (2019). The relationship between Kestel Polje system and the Antalya Tufa Plateau: their morphotectonic evolution in Isparta Angle, Antalya-Turkey. *Geomorphology* 334, 112–125. doi: 10.1016/j.geomorph.2019.03.003

Doğu, A. F., Çiçek, I., Tunçel, H., and Gürgen, G. (1999). Akdag'ın jeomorfolojisi ve bunun beşeri faaliyetler Üzerine etkisi. *Türk. Coğrafyası Araşt. Uygul. Merkezi Dergisi.* 7, 95–120.

Dortch, J. M., Owen, L. A., Haneberg, W. C., Caffee, M. W., Dietsch, C., and Kamp, U. (2009). Nature and timing of large landslides in the Himalaya and Transhimalaya of northern India. *Quat. Sci. Rev.* 28, 1037–1054. doi: 10.1016/j.quascirev.2008.05.002

Duman, T. Y. (2009). The largest landslide dam in Turkey: tortum landslide. *Eng. Geol.* 104, 66–79. doi: 10.1016/j.enggeo.2008.08.006

Dunne, J., Elmore, D., and Muzikar, P. (1999). Scaling factors for the rates of production of cosmogenic nuclides for geometric shielding and attenuation at depth on sloped surfaces. *Geomorphology* 27, 3–11. doi: 10.1016/s0169-555x(98)00086-5

Dunning, S. A., Mitchell, W. A., Rosser, N. J., and Petley, D. N. (2007). The Hattian Bala rock avalanche and associated landslides triggered by the Kashmir Earthquake of 8 October 2005. *Eng. Geol.* 93, 130–144. doi: 10.1016/j.enggeo.2007.07.003

Eastwood, W. J., Leng, M. J., Roberts, N., and Davis, B. (2007). Holocene climate change in the eastern Mediterranean region: a comparison of stable isotope and pollen data from Lake Gölhisar, southwest Turkey. *J. Quat. Sci.* 22, 327–341. doi: 10.1002/jqs.1062

Elmore, D., Ma, X., Miller, T., Nueller, K., Perry, M., Rickey, F., et al. (1997). Status and plans for the PRIME Lab AMS facility. *Nucl. Instrum. Methods Phys. Res. Sect. B Beam Interact. Mater. Atoms* 123, 69–72. doi: 10.1016/s0168-583x(96)00621-0

Emre, Ö, and Duman, T. Y. (2011). *Active Fault Map Series of Turkey, Fethiye (NJ 35-16) Quadrangle. Serial Number* 13. Ankara-Turkey: General Directorate of Mineral Research and Exploration.

Evans, J. M., Stone, J. O. H., Fifield, L. K., and Cresswell, R. G. (1997). Cresswell, Cosmogenic chlorine-36 production in potassium feldspars. *Nttcl. Lnstrttm. Methods B* 123, 334–340. doi: 10.1016/s0168-583x(96)00714-8

Fabryka-Martin, J. T. (1988). *Production of Radionuclides in the Earth and Their Hydrogeologic Significance, with Emphasis on Chlorine-36 and Iodine-129*. PhD., University of Arizona, Tucson.

Gischig, V., Amann, F., Moore, J. R., Loew, S., Eisenbeiss, H., and Stempfhuber, W. (2011). Composite rock slope kinematics at the current Randa instability, Switzerland, based on remote sensing and numerical modeling. *Eng. Geol.* 118, 37–53. doi: 10.1016/j.enggeo.2010.11.006

Görüm, T. (2019). Tectonic, topographic and rock-type influences on large landslides at the northern margin of the Anatolian Plateau. *Landslides* 16, 333–346. doi: 10.1007/s10346-018-1097-7

Görüm, T., Bayrakdar, C., Avdan, U., and Çömert, R. (2017). Geomorphology of the mount akdag landslide, western taurus range (SW Turkey). *J. Maps* 2, 165–172. doi: 10.1080/17445647.2017.1280424

Görüm, T., Korup, O., van Westen, C. J., van der Meijde, M., Xu, C., and van der Meer, F. D. (2014). Why so few? Landslides triggered by the 2002 Denali earthquake, Alaska. *Quat. Sci. Rev.* 95, 80–94. doi: 10.1016/j.quascirev.2014.04.032

Heim, A. (1932). *Bergsturz und Menschenleben. Vierteljahrschr. Naturf. Ges*. içinde Zurich: Beer and Co, 218

Hermanns, R. L., Niedermann, S., Ivy-Ochs, S., and Kubik, P. W. (2004). Rock avalanching into a landslide-dammed lake causing multiple dam failure in Las Conchas valley (NW Argentina)-evidence from surface exposure dating and stratigraphic analyses. *Landslides* 2, 113–122.

Hermanns, R. L., and Strecker, M. R. (1999). Structural and lithological controls on large Quaternary rock avalanches (sturzstroms) in arid northwestern Argentina *Geol. Soc. Am. Bull.* 111, 934–948. doi: 10.1130/0016-7606(1999)111<0934:salcol>2.3.co;2

Hewitt, K., Clague, J. J., and Orwin, J. F. (2008). Legacies of catastrophic rock slope failures in mountain landscapes. *Earth-Sci. Rev.* 87, 1–38. doi: 10.1016/j.earscirev.2007.10.002

Heyman, J., Stroeven, A. P., Harbor, J. M., and Caffee, M. W. (2011). Too young or too old: evaluating cosmogenic exposure dating based on an analysis of compiled boulder exposure ages. *Earth Planet. Sci. Lett.* 302, 71–80. doi: 10.1016/j.epsl.2010.11.040

Hilger, P., Gosse, J. C., and Hermanns, R. L. (2019). How significant is inheritance when dating rockslide boulders with terrestrial cosmogenic nuclide dating?-a case study of an historic event. *Landslides* 16, 729–738. doi: 10.1007/s10346-018-01132-0

Huggel, C., Clague, J. J., and Korup, O. (2012). Is climate change responsible for changing landslide activity in high mountains? *Earth Surf. Process. Landforms* 37, 77–91. doi: 10.1002/esp.2223

Hungr, O., and Evans, S. G. (2004). Entrainment of debris in rock avalanches; an analysis of a long run-out mechanism. *Geol. Soc. Am. Bull.* 116, 1240–1252.

Ivy-Ochs, S., Kerschner, H., and Schluchter, C. (2007). Cosmogenic nuclides and the dating of lateglacial and early holocene glacier variations: the alpine perspective. *Quat. Int.* 16, 53–63. doi: 10.1016/j.quaint.2006.12.008

Ivy-Ochs, S., Martin, S., Campedel, P., Hippe, K., Alfimov, V., Vockenhuber, C., et al. (2017). Geomorphology and age of the Marocche di Dro rock avalanches (Trentino, Italy). *Quat. Sci. Rev.* 169, 188–205. doi: 10.1016/j.quascirev.2017.05.014

Ivy-Ochs, S., Poschinger, A. V., and Maisch, M. (2009). Surface exposure dating of the Flims landslide, Graubunden, Switzerland. *Geomorphology* 103, 104–112. doi: 10.1016/j.geomorph.2007.10.024

Ivy-Ochs, S., and Schaller, M. (2010). Examining processes and rates of landscape change with cosmogenic radionuclides. *Radioact. Environ.* 16, 231–294. doi: 10.1016/s1569-4860(09)01606-4

Ivy-Ochs, S., Synal, H. A., Roth, C., and Schaller, M. (2004). Ivy-Ochs, S., Synal, Initial results from isotope dilution for Cl and Cl-36 measurements at the PSI/ETH Zurich AMS facility. *Nucl. Instrum. Methods Phys. Res. Sect. B Beam Interact. Mater. Atoms* 223–224, 623–627. doi: 10.1016/j.nimb.2004.04.115

Keefer, D. K. (1984). Rock avalanches caused by earthquakes: source characteristics. *Science* 223, 1288–1290. doi: 10.1126/science.223.4642.1288

Korup, O. (2002). Recent research on landslide dams - a literature review with special attention to New Zealand. *Prog. Phys. Geogr. Earth Environ.* 26, 206–235. doi: 10.1191/0309133302pp333ra

Korup, O., Clague, J. J., Hermanns, R. L., Hewitt, K., Strom, A. L., and Weidinger, J. T. (2007). Giant landslides, topography, and erosion. *Earth Planet. Sci. Lett.* 261, 578–589. doi: 10.1016/j.epsl.2007.07.025

Korup, O., and Dunning, S. (2015). "Catastrophic mass wasting in high mountains," in *The High-mountain Cryosphere*, eds C. Huggel, M. Carey, and J. J. Clague (Cambridge: Cambridge University Press), 127–146. doi: 10.1017/cbo9781107588653.008

Korup, O., Schmidt, J., and McSaveney, M. J. (2005). Regional relief characteristics and denudation pattern of the western Southern Alps, New Zealand. *Geomorphology* 71, 402–423. doi: 10.1016/j.geomorph.2005.04.013

Kotthoff, U., Pross, J., Muller, U. C., Peyron, O., Schmiedl, G., Schulz, H., et al. (2008). Climate dynamics in the borderlands of the Aegean Sea during formation of sapropel S1 deduced from a marine pollen record. *Quat. Sci. Rev.* 27, 832–845. doi: 10.1016/j.quascirev.2007.12.001

Lal, D. (1991). Cosmic ray labeling of erosion surfaces: in situ nuclide production rates and erosion models. *Earth Planet. Sci. Lett.* 104, 424–439. doi: 10.1016/0012-821x(91)90220-c

Liu, B. L., Phillips, F. M., Fabrykamartin, J. T., Fowler, M. M., and Stone, W. D. (1994). Cosmogenic 36Cl accumulation in unstable landforms, 1. Effects of the thermal neutron distribution. *Water Resour. Res.* 30, 3115–3125. doi: 10.1029/94wr00761

Marino, G., Rohling, E. J., Sangiorgi, F., Hayes, A., Casford, J. L., Lotter, A. F., et al. (2009). Early and middle Holocene in the Aegean Sea: interplay between high and lowlatitude climate variability. *Quat. Sci. Rev.* 28, 3246–3262. doi: 10.1016/j.quascirev.2009.08.011

McColl, S. T. (2012). Paraglacial rock-slope stability. *Geomorphology* 15, 1–16. doi: 10.1016/j.geomorph.2012.02.015

McColl, S. T. (2015). "Landslide causes and triggers," in *Landslide Hazards, Risks and Disasters*, eds T. Davies and N. Rosser (Amsterdam: Elsevier Science), 17–42. doi: 10.1016/b978-0-12-396452-6.00002-1

McColl, S. T., and Davies, T. R. H. (2013). Large ice-contact slope movements: glacial buttressing deformation and erosion. *Earth Surf. Process. Landf.* 38, 1102–1115. doi: 10.1002/esp.3346

Nazik, L., Poyraz, M., and Karabıyıkoğlu, M. (2019). "Karstic landscapes and landforms in Turkey," in *Landscapes and Landforms of Turkey*, eds C. Kuzucuoğlu and A. Çiner (Cham: Springer), 181–196. doi: 10.1007/978-3-030-03515-0_5

Nazik, L., and Tuncer, K. (2010). Türkiye karst morfolojisinin bölgesel özellikleri. *Türk. Speleol. Dergisi* 1, 7–19.

Nichols, K. K., Bierman, P. R., Foniri, W. R., Gillespie, A. R., Caffee, M., and Finkel, R. (2006). Dates and rates of arid region geomorphic processes. *Geol. Soc. Am. Today* 16, 4–11.

Ocakoğlu, F., Kır, O., Yılmaz, ÝÖ, Açıkalın, S., Erayık, C., Tunoğlu, C., et al. (2013). Early to mid-holocene lake level and temperature records from the terraces of lake sünnet in NW Turkey. *Palaeogeogr. Palaeoclimatol. Palaeoecol.* 369, 175–184. doi: 10.1016/j.palaeo.2012.10.017

Olaya, V., and Conrad, O. (2009). "Chapter 12 geomorphometry in SAGA," in *Geomorphometry – Concepts, Software, Applications*, eds T. Hengl and H. I. Reuter (Amsterdam: Elsevier), 293–308. doi: 10.1016/s0166-2481(08)00012-3

Onde, H. (1952). "Formes Glaciaires dans le Massif Lycien de I'Akdağ," in *XIXe Congres Geologique International, Alger Fasc. XV* (Algiers: Association des Services Geologiques Africains Press), 327–335.

Pánek, T. (2015). Recent progress in landslide dating: a global overview. *Progr. Phys. Geogr. Earth Environ.* 39, 168–198. doi: 10.1177/0309133314550671

Pánek, T. (2019). Landslides and quaternary climate changes—The state of the art. *Earth-Sci. Rev.* 196, 102871. doi: 10.1016/j.earscirev.2019.05.015

Phillips, F. M., Stone, W. D., and Fabryka-Martin, J. T. (2001). An improved approach to calculating low-energy cosmic-ray neutron fluxes near the land/atmosphere interface. *Chem. Geol.* 175, 689–701. doi: 10.1016/s0009-2541(00)00329-6

Planhol, X., and İnandık, H. (1958). La limite de la glaciation quaternaire dans le massif du yeşil göl dağ (anatolie du sud-quest). *Review* 4, 33–35.

Prager, C., Ivy-Ochs, S., Ostermann, M., Synal, H., and Patzelt, G. (2009). Geology and dating of the Fernpass rockslide (Tyrol, Austria). *Geomorphology* 103, 93–103. doi: 10.1016/j.geomorph.2007.10.018

Putkonen, J., and Swanson, T. (2003). Accuracy of cosmogenic ages for moraines. *Quat. Res.* 59, 255–261. doi: 10.1016/s0033-5894(03)00006-1

Samartin, S., Heiri, O., Joos, F., Renssen, H., Franke, J., Brönnimann, S., et al. (2017). Warm Mediterranean mid-Holocene summers inferred from fossil midge assemblages. *Nat. Geosci.* 10, 207–212. doi: 10.1038/ngeo2891

Sarıkaya, M. A., and Çiner, A. (2015). Türkiye Geç Pleyistosen Buzullaşması ve Paleoiklimi. *Maden Tetkik ve Arama Dergisi* 151, 111–132.

Sarıkaya, M. A., Çiner, A., Haybat, H., and Zreda, M. (2014). An early advance of glaciers on Mount Akdağ, SW Turkey, before the global Last Glacial Maximum; insights from cosmogenic nuclides and glacier modeling. *Quat. Sci. Rev.* 88, 96–109. doi: 10.1016/j.quascirev.2014.01.016

Sarıkaya, M. A., Ciner, A., and Yıldırım, C. (2017). Cosmogenic S 36Cl glacial chronologies of the Late Quaternary glaciers on Mount Geyikdag in the eastern Mediterranean. *Quat. Geochronol.* 39, 189–204. doi: 10.1016/j.quageo.2017.03.003

Şenel, M. (1997). *1/100.000 ölçekli Türkiye Jeoloji Haritaları, Fethiye-L9 paftası*. Ankara: MTA.

Shakun, J. D., and Carlson, A. E. (2010). A global perspective on Last Glacial Maximum to Holocene climate change. *Quat. Sci. Rev.* 29, 1801–1816. doi: 10.1016/j.quascirev.2010.03.016

Shulmeister, J., Davies, T. R., Evans, D. J. A., Hyatt, O. M., and Tovar, D. S. (2009). Catastrophic landslides, glacier behaviour and moraine formation – A view from an active plate margin. *Quat. Sci. Rev.* 28, 1085–1096. doi: 10.1016/j.quascirev.2008.11.015

Singeisen, C., Ivy-Ochs, S., Wolter, A., Steinemann, O., Akçar, N., Yesilyurt, S., et al. (2020). The Kandersteg rock avalanche (Switzerland): integrated analysis of a late Holocene catastrophic event. *Landslides* 17, 1297–1317. doi: 10.1007/s10346-020-01365-y

Smith, K. (2001). *Environmental Hazards: Assessing Risk and Reducing Disaster*, Third Edn. London: Routledge.

Stead, D., and Wolter, A. (2015). A critical review of rock slope failure mechanisms: the importance of structural geology. *J. Struct. Geol.* 74, 1–23. doi: 10.1016/j.jsg.2015.02.002

Stone, J., Evans, J., Fifield, K., Cresswell, R., and Allan, G. L. (1996). Cosmogenic chlorine-36 production rates from calcium and potassium: radiocarbon. *Radiocarbon* 38, 170–171.

Stone, J. O. (2000). Air pressure and cosmogenic isotope production. *J. Geophys. Res. Solid Earth* 105 23753–23759. doi: 10.1029/2000jb900181

Stone, J. O. H., Evans, J. M., Fifield, L. K., Allan, G. L., and Cresswell, R. G. (1998). Cosmogenic chlorine-36 production in calcite by muons. *Geochim. Cosmochim. Acta* 62, 433–454. doi: 10.1016/s0016-7037(97)00369-4

Strom, A. L., and Korup, O. (2006). Extremely large rockslides and rock avalanches in the Tien Shan Mountains, Kyrgyzstan *Landslides* 3, 125–136. doi: 10.1007/s10346-005-0027-7

Synal, H. A., Bonani, G., Ender, R. M., Gartenmann, P., Kubik, P. W., Schnabel, C., et al. (1997). Status report of the PSI/ETH AMS facility. *Nucl. Instrum. Methods Phys. Res. Sect. B Beam Interact. Mater. Atoms* 123, 62–68. doi: 10.1016/s0168-583x(96)00608-8

Tanyas, H., Van Westen, C. J., Allstadt, K. E., Jessee, M. A. N., Gorum, T., Jibson, R. W., et al. (2017). Presentation and analysis of a worldwide database of earthquake-induced landslide inventories. *J. Geophys. Res. Earth Surf.* 122, 1991–2015. doi: 10.1002/2017jf004236

Ten Veen, J. H. (2004). Extension of Hellenic forearc shear zones in SW Turkey: the Pliocene–Quaternary deformation of the Eşe Çay Basin. *J. Geodynam.* 3, 181–204. doi: 10.1016/j.jog.2004.02.001

Ulusay, R., Tuncay, E., Sonmez, H., and Gokceoglu, C. (2004). An attenuation relationship based on Turkish strong motion data and iso-acceleration map of Turkey. *Eng. Geol.* 74, 265–291. doi: 10.1016/j.enggeo.2004.04.002

Weidinger, J. T., Wang, J., and Ma, N. (2002). The earthquake-triggered rock avalanche of Cui Hua, Qin Ling Mountains, PR of China—the benefits of a lake-damming prehistoric natural disaster. *Quat. Int.* 93, 207–214. doi: 10.1016/s1040-6182(02)00019-8

Wells, D., and Coppersmith, K. (1994). New empirical relationships among magnitude, rupture length, rupture width, rupture area, and surface displacement. *Bull. Seismol. Soc. Am.* 84, 974–1002.

Conflict of Interest: The authors declare that the research was conducted in the absence of any commercial or financial relationships that could be construed as a potential conflict of interest.